

Analysis of integrated heating approaches for cold-start conditions in 21700 lithium-ion battery modules
using thermal system simulation

by

Grace Stephanie Parra Panchi

A thesis

presented to the University of Waterloo

in fulfillment of the

thesis requirement for the degree of

Master of Applied Science

in

Chemical Engineering

Waterloo, Ontario, Canada, 2025

© Grace Stephanie Parra Panchi 2025

Author's Declaration

I hereby declare that I am the sole author of this thesis. This is a true copy of the thesis, including any required final revisions, as accepted by my examiners.

I understand that my thesis may be made electronically available to the public.

Abstract

Cold ambient conditions significantly reduce discharge capacity and slow the thermal response of lithium-ion cells, particularly at low state of charge (SOC). To address these challenges, this research studies the feasibility of heating strategies to improve cold-start performance in 21700 lithium-ion battery modules using thermal system simulation. Both experimental and simulation-based approaches were employed. At the cell level, experimental tests were conducted to evaluate thermal and capacity behavior under sub-zero temperatures. These results were compared against thermal system simulation simulations under convective or adiabatic conditions, revealing that real-world test setups introduce additional resistances not captured in idealized models. And adiabatic conditions could allow faster cell heating compared to convective conditions due to internal heat accumulation, which shows the effect of insulation. In fact, the temperature rise simulated under adiabatic conditions is approximately 2.3–2.9 times greater than under simulated convective conditions. Building on these findings, a module design was developed to enable system-level simulation of thermal strategies. The design considered safety, structural integrity, and thermal performance, balancing insulation with heat flow pathways. Then the study focuses on evaluating the feasibility of external and battery-powered heating strategies. Four heating configurations were simulated, external heating, battery discharge, or combined configurations. Simulations were carried out across below zero ambient temperatures of $-20\text{ }^{\circ}\text{C}$, $-10\text{ }^{\circ}\text{C}$, and $0\text{ }^{\circ}\text{C}$ and different initial SOC values of 80%, 50% and 20%. Results show that in the absence of heating, the battery was unable to complete discharge at low SOC, particularly at $-20\text{ }^{\circ}\text{C}$ and 20% initial SOC. Yet when external surface heating was applied, the module achieved a faster temperature rise enabling full discharge even under these extreme conditions. Furthermore, when external heating is applied without discharge, the heating rate slows down, highlighting the added benefit of internal heat generation during battery operation. Lastly, the study evaluated whether the battery could power its own heating system. At 20% SOC and $-20\text{ }^{\circ}\text{C}$, the energy required for heating exceeded the battery's usable output, rendering self-heating unfeasible. In contrast, at $0\text{ }^{\circ}\text{C}$ and moderate SOC levels, it remained viable, with heating demands as low as 2 - 3% of the available capacity.

Overall, the findings support the integration of targeted heating strategies into electric vehicle (EV) thermal management systems, showing that a combination of external heating and internal heat generation enables reliable cold-start performance while minimizing energy consumption for battery heating in sub-zero conditions.

Acknowledgements

The author acknowledges the Battery Workforce Challenge (BWC), along with its headline sponsors the U.S. Department of Energy and Stellantis, and Argonne National Laboratory, for making this impactful academic and technical journey possible. Their support created a valuable opportunity to engage in hands-on battery research and innovation within a real-world engineering framework.

The author also acknowledges the support provided by AVL and Batemo. Access to simulation software, including AVL CRUISE™M, AVL FIRE™M and the Batemo Cell Model, was essential to the development of thermal and electrochemical simulations. Their provision of modeling data and responsive technical assistance significantly contributed to the progress and depth of the analysis.

Gratitude is extended to the Natural Sciences and Engineering Research Council of Canada (NSERC) for their funding and support of research initiatives.

The author is deeply thankful to the University of Waterloo, and to every member of the University of Waterloo - Lambton College (UWLC) team, whose dedication and collaboration made this experience truly rewarding. Heartfelt thanks go to her supervisors: Dr. XiaoYu Wu for his dedicated supervision and mentorship throughout the research journey and Dr. Yverick Rangom for securing the funding that made this project possible. Special recognition is owed to the members of the Greener Production Group for fostering a collaborative research environment.

Finally, the author expresses her deepest gratitude to her family, Adriana, Oswaldo, and Andrea, for their unconditional love and support across distance and time.

Dedication

A mis extraordinarios padres Oswaldo y Adriana; a mi amada hermana Andrea y a mi angelito, mi abuelita Inés, por enseñarme el verdadero valor del sacrificio y la perseverancia.

“It’s not so important who starts the game but who finishes it”

John Wooden

Table of Contents

Author’s Declaration	ii
Abstract.....	iii
Acknowledgements.....	iv
Dedication	v
List of Figures.....	x
List of Tables	xii
List of Abbreviations.....	xiii
Chapter 1 Introduction.....	1
1.1 Context and Motivation.....	1
1.2 Research Problem Definition.....	2
1.3 Objectives and Scope.....	2
1.4 Thesis Structure	3
Chapter 2 Literature Review.....	4
2.1 Battery Thermal Behavior.....	4
2.1.1 Lithium-ion battery system fundamentals.....	4
2.1.2 Temperature-Dependent Mechanisms in Lithium-Ion Battery Systems	5
2.1.3 Module level performance.....	7
2.2 Existing Heating Strategies.....	8
2.3 Simulation and Modeling Techniques.....	9
2.4 Gaps in Current Research	10
Chapter 3 Cell Characterization and Thermal Behavior at Low Temperatures.....	12
3.1 Introduction.....	12
3.2 Experimental Methodology.....	12

3.2.1 Test Setup.....	12
3.2.2 Test Procedure.....	14
3.3 Simulation methodology.....	15
3.3.1 Model configuration overview.....	15
3.3.2 Discharge simulation with a convective thermal model	16
3.3.3 Discharge simulation under adiabatic conditions.	17
3.4 Results.....	17
3.4.1 Capacity Behavior at Cold Temperatures	17
3.4.2 Thermal Response at Cold Start Conditions.....	24
3.5 Summary of Findings.....	29
Chapter 4 Conceptual Module Design Basis for Thermal Simulation.....	31
4.1 Introduction.....	31
4.2 Design considerations	31
4.2.1 Thermal management requirements.....	31
4.2.2 Structural considerations and geometric constraints	32
4.2.3 Material assessment criteria	32
4.3 Design Description.....	33
4.3.1 Top cover.....	34
4.3.2 Top cell holder.....	35
4.3.3 Module walls.....	36
4.3.4 Cells.....	37
4.3.5 Bottom cell holder.....	38
4.3.6 Bottom cover.....	39
4.4 Lessons Learned and Design Limitations	41

4.5 Summary of Findings.....	41
Chapter 5 Simulation and Analysis of Heating Strategies for the Battery Module.....	43
5.1 Introduction.....	43
5.2 Simulation model development.....	43
5.2.1 Simulation environment.....	43
5.2.2 Module Geometry and Simplification Strategy.....	44
5.2.3 Simulation model without heating elements.....	44
5.2.4 Simulation model with external heating at the top cover.....	46
5.2.5 Model assumptions and limitations.....	47
5.3 Methodology for evaluating heating integration strategies.....	47
5.4 Results - Cold discharge with and without external heating.....	48
5.4.1 Temperature rise profile at different ambient temperatures.....	48
5.4.2 Final SOC's at different ambient temperatures.....	53
5.5 Results - Heating behavior with and without battery discharge.....	54
5.6 Results - Battery-Powered Heating Feasibility.....	56
5.6.1 Effect/Feasibility of self – heating.....	56
5.7 Design implications and future work.....	58
5.8 Summary of findings.....	58
Chapter 6 Conclusions and Recommendations.....	60
6.1 Key Findings.....	60
6.2 Limitations.....	61
6.3 Recommendations for Future Work.....	62
References.....	63
Appendix A MACCOR Test Sequence.....	68

Appendix B OCV vs SOC curve.....	69
Appendix C Module Electrical Configuration.....	70

List of Figures

Figure 1. Experimental setup for battery cell testing	13
Figure 2. Device under test a) Overview of the test connections b) Cell set up.....	14
Figure 3. Current and voltage profiles of the capacity test applied to the 21700 lithium-ion cell.....	15
Figure 4. Configuration of the battery cell discharge simulation setup under convective conditions..	16
Figure 5. Configuration of the battery cell discharge simulation setup under adiabatic conditions	17
Figure 6. Discharge curves of a 21700 lithium-ion cell at different ambient temperatures for (a) experimental results, (b) simulations under convective conditions, and (c) simulations under adiabatic conditions, all at a 1C discharge rate (4.9 A).....	18
Figure 7. Discharge voltage curves of a 21700 lithium-ion cell at different ambient temperatures, segmented by SOC zones and compared with the reference ECM for (a) experimental results and (b) simulations under convective conditions.	21
Figure 8. Surface temperature plots of a 21700 lithium-ion cell as a function of SOC for (a) experimental data, (b) simulation with convective conditions, and (c) simulations under adiabatic conditions, at -12 °C, -3 °C, 11 °C, and 30 °C and at 1C discharge rate (4.9 A).....	25
Figure 9. Surface temperature rise (ΔT) of a 21700 lithium-ion cell as a function of SOC for (a) experimental results, (b) simulations with convective conditions, and (c) simulations under adiabatic conditions, at -12 °C, -3 °C, 11 °C, and 30 °C under a 1C discharge rate (4.9 A).....	27
Figure 10. Battery module design	33
Figure 11. Isometric view of the battery module top cover.....	34
Figure 12. Isometric view of the battery module top cell holder.....	35
Figure 13. Isometric view of the battery module walls	36
Figure 14. Isometric view of the battery module cell block	37
Figure 15. Isometric view of the battery module bottom cover	38
Figure 16. Heat transfer path from the cell base to the cooling plate through the TIM layer and bottom cover.....	39
Figure 17. Isometric view of the battery module bottom cover	40
Figure 18. Battery module geometry used for simulation: (a) Simplified homogenized model used for thermal analysis, (b) Detailed configuration showing a simplified meshed structure and internal cell layout.....	43
Figure 19. Simulation model configuration showing boundary conditions and component interactions for the unheated cold start scenario.	44

Figure 20. Simulation model configuration showing boundary conditions and component interactions for the heated cold start scenario.....	46
Figure 21. Visual representation of the four simulated heating configurations. HE: Heating Elements; CP: Cooling Plate. "On" indicates battery operation; "Off" indicates no discharge.....	48
Figure 22. Surface temperature evolution of a 21700 lithium-ion cell for Case A: no heating and Case B: external heating, under cold-start conditions at initial SOC levels of (a) 80%, (b) 50%, and (c) 20%, and ambient temperatures of -20 °C, -10 °C, and 0 °C.....	49
Figure 23. Evolution of temperature distributions over time at -20 °C and 50% initial SOC for (a) Case A and (b) Case B. The walls are hidden to visualize the effect on the 21700 cells block.	52
Figure 24. MACCOR test sequence used for static capacity testing of 21700 li-ion cells at 0 °C.....	68
Figure 25. Measured OCV versus SOC curve obtained from a C/20 discharge of a Samsung 21700 li-ion cell.	69
Figure 26. Electrical configuration of a 10s26p cylindrical cell battery module.....	70

List of Tables

Table 1. 21700 Battery Cell Specifications.....	13
Table 2. Capacity results of a 21700 li-ion cell discharged at 1C rate (4.9 A) at different ambient temperatures.....	22
Table 3. OCV results of a 21700 Li-ion cell discharged at 1C rate (4.9 A) at different ambient temperatures.....	23
Table 4. Initial voltage drop of a 21700 Li-ion cell discharged at 1C rate (4.9 A) at different ambient temperatures.....	24
Table 5. Final surface temperature of a 21700 Li-ion cell discharged at 1C rate (4.9 A) at different ambient temperatures.....	26
Table 6. Comparison of surface temperature rise (ΔT) between experimental results and simulations under convective (Case C) and adiabatic (Case A) conditions for different initial ambient temperatures.....	29
Table 7. Simulation components, descriptions and assigned parameter values for the unheated cold start scenario.....	45
Table 8. Description of the four simulated heating scenarios applied to the battery module.....	47
Table 9. Comparison of module heating time to reach 10 °C with and without external heating at different ambient temperatures (-20 °C, -10 °C, 0 °C) for 80%, 50% and 20% initial SOC.....	51
Table 10. Comparison of SOC decrease during cold operation with and without heating for initial SOC of 20%, 50%, and 80% at different ambient temperatures (-20 °C, -10 °C, and 0 °C).....	53
Table 11. Comparison of module heating time to reach 10 °C with external preheating (no operation) and external heating during cold operation at ambient temperatures of -20 °C, -10 °C, and 0 °C.....	55
Table 12. Comparison of required energy to power the heating elements and usable battery energy at different ambient temperatures and initial SOC levels.....	57

List of Abbreviations

EV	Electric Vehicle
FMU	Functional Mock-up Unit
OCV	Open Circuit Voltage
PC	Polycarbonate
PCM	Phase Changing Materials
SOC	State of Charge (%)
T_s	Surface Temperature (°C)
TIM	Thermal Interface Material
TMS	Thermal Management System
ΔT	Temperature rise (°C)

Chapter 1

Introduction

1.1 Context and Motivation

The transportation sector has been undergoing significant transformation by moving away from traditional fossil fuel-based vehicles towards the increasing development of electric vehicles (EVs). EVs present a viable alternative towards more sustainable transportation due to their inherent zero-emissions operation and energy-efficient design. At the core of EVs performance are batteries, which generate electrical energy from chemical reactions when discharging and reverse the process during charging. Among different technologies, lithium-ion batteries are one of the most common power sources of EVs due to their strong power output, reduced self-discharge, high energy density, and extended lifespan [1]. For a battery pack, efficient battery thermal management systems (TMS) are critical to maintain optimal battery conditions while considering cost, weight, and volume constraints. There is a large body of experimental and simulation-based work that has been conducted over the past decade on this topic, as highlighted by [2].

Despite these advancements in TMS research, there has been limited exploration into optimizing battery lifecycles when operating at temperatures outside their ideal thermal conditions. Especially in regions with extreme climates, this gap presents a pivotal area of investigation for developing robust EV TMSs that can ensure reliable performance for everyday use. Canada is a particularly relevant case, as it faces the dual reality of an ambitious national goal: the Canadian government has committed to transitioning to 100% emission-free new light-duty vehicles by 2035 [3], and harsh winter conditions as in parts of the country temperature can drop below -40°C . This poses challenges, as at lower temperatures, the lithium-ion battery components suffer several changes including reduced kinetic and mass transport rates, thickening of the electrolyte and higher risk of metallic lithium accumulation, a process known as lithium plating [4]. These changes can lead to lower total energy available, lower power output and increased internal resistance, thus, affecting EV performance, speeding up battery wear and shortening its lifespan [4]. Gaining a deeper understanding of extended temperature operation would not only strengthen market opportunities but also ensure the real-world applicability of EVs.

One approach to overcoming these cold temperature limitations is to restore the optimal conditions for temperature-dependent processes by preheating the EV's power source, i.e., the battery pack. Several aspects need to be taken into consideration for this approach such as energy consumption of the heating,

the time required to reach optimal operating temperatures and the overall complexity of the TMSs. Additionally, cooling must also be considered, as its primary function is to mitigate excessive temperature rise and thereby reduce the risk of thermal runaway, typically through mechanisms that involve a coolant fluid in contact with the batteries, as summarized by [5]. Therefore, this study focuses on developing a thorough understanding of hybrid (heating and cooling) TMS for lithium-ion battery modules and its suitability for EV applications.

1.2 Research Problem Definition

The operation of lithium-ion batteries under low temperature conditions remains a major challenge for EV performance that hinders user acceptance. Although existing technologies support basic functionality in cold environments, they often lack fast response thermal management solutions. This limitation is especially critical at low states of charge (SOC), where lithium-ion cells experience more pronounced capacity loss. Hence, there is a need for a TMS capable of rapidly heating the battery to optimal operating temperatures under these demanding conditions. This study addresses that gap by exploring an integrated heating and cooling strategy at the module level.

1.3 Objectives and Scope

The main objective of this thesis is to develop a module-level EV thermal management system for 21700 lithium-ion batteries, combining cell-level thermal characterization, module mechanical and thermal considerations, and the integration of a targeted heating strategy to improve cold-start performance.

To achieve this, the first step involves modeling the thermal behavior of the module under low-temperature conditions by integrating electric heating and a bottom cooling plate. The second objective is to evaluate the effect of different initial SOC levels on the thermal response and power loss characteristics of the battery module. The third objective is to analyze how variations in heater power influence the warm-up time and temperature distribution within the module under varying SOC conditions.

The scope of this study is limited to the thermal analysis at the module level considering uniform cell behavior.

1.4 Thesis Structure

This thesis is organized into five chapters. Chapter 1 introduces the context, motivation, and importance of improving cold-start performance in lithium-ion battery modules, particularly in EV applications. It also defines the research problem, outlines the objectives and scope and provides an overview of the thesis structure. Chapter 2 presents a review of the relevant literature, including current knowledge on battery thermal behavior, heating strategies, and simulation techniques, while identifying gaps in the existing research. Chapter 3 focuses on the experimental and simulation-based characterization of 21700 lithium-ion cells at low temperatures. It details the test procedures, model configurations, and analyzes both capacity and thermal behavior. Chapter 4 presents the conceptual design of a battery module developed to support thermal simulations. It follows a component-level approach, including material selection and design rationale. Finally, Chapter 5 integrates the cell-level insights into a module-level thermal model. It evaluates the effects of heating strategies on a module exposed to different ambient temperatures and SOCs.

Chapter 2

Literature Review

The adoption of EV's as an alternative to fuel-based transportation largely depends on the performance, lifespan, and safety of their power source: the battery pack. Due to their electrochemical nature, lithium-ion batteries are highly sensitive to temperature. One of the main concerns is their reduced performance and potential degradation when operated at low temperatures. This literature review will examine the known issues associated with lithium-ion batteries under cold conditions and explore existing battery thermal management strategies for EV operating below freezing. It will also assess the validity of the simplified one-dimensional battery simulation approach and highlight the research gaps that this study aims to address.

2.1 Battery Thermal Behavior

2.1.1 Lithium-ion battery system fundamentals

Understanding how battery systems are structured is essential to addressing their performance and safety challenges. A battery system starts with a cell as the fundamental electrochemical unit. A group of cells connected in series or parallel constitute a battery module. This module functions as a self-contained unit with electrical and mechanical autonomy [6]. Finally, a collection of modules connected in series or parallel constructs a complete battery pack [6]. This modular construction provides the required voltage and capacity for EV applications.

Among available technologies, lithium-ion batteries have emerged as the dominant choice for EV battery packs due to their high energy density, strong power output, extended lifespan, reduced self-discharge and cost-efficiency [7]. For example, 21700 lithium ion cells are widely used as cells for the Tesla models [8], [9]. This cylindrical cell consists of a separating electrolyte layer placed between an aluminum foil covered positive electrode (cathode) and a copper coated negative electrode (anode) as shown by [10]. Highlighting the external structure of a cylinder, [10] shows a 3.6 V, 1.5 Ah cylindrical lithium-ion cell where a cross-section reveals internal layers of carbon on copper (Cu), lithium manganese oxide ($\text{Li}_x\text{Mn}_2\text{O}_4$) on aluminum (Al), a separator, and liquid electrolyte, all enclosed in a cell can. This shows that the layers are stacked together to form an electrochemical unit.

2.1.2 Temperature-Dependent Mechanisms in Lithium-Ion Battery Systems

Due to the electrochemical nature of lithium-ion batteries, many of the operating mechanisms are temperature dependent. The rate at which a general lithium-ion battery charges/discharges depends on two temperature-dependent processes: the rate of the chemical reactions at the electrodes and the speed at which lithium ions move within the battery [11]. The first process is driven by the kinetics of the charge transfer reactions meaning that the battery performance is dependent on the electrochemical conversion speed [11]. According to the Arrhenius law, an increase in temperature leads to an exponential surge in the rate of chemical reactions. The second process is dominated by the mass transfer of lithium ions. In other words, the battery is waiting for enough lithium ions to diffuse through the electrolyte layer to get to the reaction sites [11]. Moreover, the internal resistance of the battery is affected by temperature which in turn directly affects the voltage input, power output and heat generation of the battery during operation. Side-reactions are also more likely to occur at extreme temperatures which can result in changing material characteristics, creating hazardous conditions and/or accelerating aging of the battery components [10] [7].

As indicated in [12], the optimal performance of lithium-ion batteries is achieved when operated at temperatures between 15°C and 35°C. A direct consequence at temperatures that are either above or below their ideal range is a change in their electrochemical and temperature-dependent processes, as summarized in [10], since at low temperatures lithium-ion batteries face multiple challenges that degrade performance and increase safety risks.

[10] noted that electrolyte viscosity rises and ionic conductivity decreases, reducing Li^+ mobility and slowing solid-state diffusion, which may hinder electrochemical processes. In addition, [10] highlights that the resistance of the solid electrolyte interphase increases, which could promote Li-plating, dendrite formation, and internal short circuits, compromising safety. These consequences rise because in the ideal electrochemical reaction, the capacity relates to the number of lithium ions participating in the electrode reactions, and the voltage corresponds to the energy available due to the potential difference between the anode and cathode [10]. As such, [10] shows that the battery TMS employs heating and cooling techniques to restore optimal operation conditions, thereby ensuring safer battery use in electric vehicles.

To characterize the battery's performance, the charging and discharging operation of a lithium-ion battery can be represented in different plots. As such, [10] summarizes in four plots the electrochemical

performance of a lithium-ion cell. In the first plot, [10] shows voltage versus capacity at different discharge rates ranging from 0.2 C to 3 C. In this plot, it is revealed that as the C-rate increases, the discharge profiles shift and the delivered capacity decreases. [10] then presents a second plot of the discharge ratio as a function of temperature, using a charge at 1 C with a cut-off voltage of 4.2 V at 25 °C and a discharge at 1 C with a cut-off voltage of 2.5 V at 25 °C, showing that the discharge ratio increases with temperature from below 40% at -30 °C to nearly 100% at around 40 °C. In a third plot, [10] presents two voltage–capacity curves at -10 °C and -20 °C, again under the charge condition of CC/CV, 1 C, 4.2 V at 25 °C. This plot shows that lowering the temperature to -10 °C shifts the curve to lower voltages and results in reduced capacity. This reduction is influenced by the slowdown in electrochemical reaction kinetics which affect the battery's efficiency in delivering energy [10]. Also, the electrolyte could become more viscous thereby reducing the ion flow speed [7]. Through this comparison, it can be highlighted that there is a strong effect of subzero temperatures in reducing capacity as the temperature decreases. Lastly, [10] reports in a fourth plot the cycling stability under the same charge and discharge conditions, showing that capacity decreases gradually with cycle number, with a retention of 92.6% after 400 cycles.

This conclusion has been supported by several studies summarized in [13], which indicate that low temperatures negatively impact battery performance by increasing internal resistance and lowering discharge capacity. These effects ultimately compromise the driving performance of EVs. In extreme cases, cold conditions may even prevent vehicle start-up.

Additionally, the use of lithium-ion batteries in cold temperatures can also change the intrinsic properties of battery components. Lithium plating can lead to extended battery damage due to unwanted formation of metallic lithium on the anode. This can then develop into internal short circuits from the formation of lithium dendrites on the electrode surface. Thus, resulting in battery malfunction and even excessive heat generation [11].

On the other hand, at elevated temperatures, research has shown there is accelerated degradation and an increased risk of system failure involving fire or explosion known as thermal runaway [11]. Additionally, the cycling performance of Li-ion batteries drops at temperatures greater than 50°C [7]. Therefore, research also focused on cooling strategies for battery systems [14]. Therefore, a wider known conclusion presented by [15] is that to maintain proper operation of battery modules, a flexible TMS is required to provide heating in cold conditions and cooling in high temperatures.

In general, effective cooling systems are needed to minimize temperature differences during operation. Therefore, maintaining balanced temperatures in lithium-ion batteries is essential. Managing temperature changes in cylindrical cells presents a different kind of challenge compared to pouch and prismatic cells. Cylindrical cells exhibit higher thermal conductivity in the axial direction than in the radial direction due to their jelly roll structure, which leads to anisotropic thermal behavior [16]. Moreover, research has shown that the high vertical thermal conductivity of cylindrical cells allows for even temperature distribution. This makes them well suited for indirect cooling methods such as bottom cooling [17].

2.1.3 Module level performance

As lithium-ion cells are combined into modules, the electrical combination of cells in series and parallel configurations increases voltage and current capacity, thereby enhancing power density. [7] illustrates the variation of power density with depth of discharge (DOD) for both a single cell and a battery module.

At low DOD values, [7] shows that the power density is at its highest, reaching approximately 1000 W/kg for the module and around 900 W/kg for the single cell. As the DOD increases, a steady decline in power density is observed for both cases, with the module consistently maintaining slightly higher values than the single cell across the entire range [7]. Beyond 60% DOD, the decrease becomes more pronounced, and by around 80 to 90% DOD, the power density for both configurations drops sharply to below 300 W/kg [7]. This behavior highlights the impact of depth of discharge on power performance and shows that modules can provide a modest advantage over individual cells.

In summary, the transition from individual lithium-ion cells to full battery modules brings both performance gains and added complexity. As EV adoption continues to grow, addressing these multi-scale challenges will be key to optimizing battery design for low-temperature conditions, enhancing performance, and ensuring safety.

A battery module should provide structural protection, support thermal management, and ensure safety under various operating conditions. In line with these requirements, the casing must be lightweight to reduce the overall mass of the pack, while also offering good impact resistance to protect the cells from mechanical stress and accidental damage [18]. Inside the module, cylindrical cells should be arranged with adequate spacing to promote airflow and support effective thermal management, while internal bracing should be incorporated to protect the cells from lateral forces during vehicle motion [18]. The

overall design objective is to maximize the mass of cells within each battery module to enhance its energy capacity [19].

2.2 Existing Heating Strategies

Several strategies have been explored to address the challenge of heating lithium-ion batteries under low-temperature conditions. Review studies [13] have categorized heating strategies as either internal or external to the battery. Internal methods include self-heating, which utilizes the cell's own resistance during charge or discharge to generate heat, and pulse heating, where alternating charging and discharging between cell groups produces internal heat [13]. Whereas external strategies are more diverse and involve applying heat outside the cell casing. These include electric heating elements placed around the cells, fluid systems circulating heated liquid nearby, and convective heating using warm air within the module [13]. Additional approaches operate at the module level, such as external electric or fluid heating and forced warm air convection [13].

Overall, study [20] has concluded that while preheating is essential to restore capacity and support high-rate operation in cold environments, no existing method fully satisfies the combined demands of efficiency, safety, cost, and uniformity. External heating methods are technically simple but suffer from inefficient heat transfer, while internal heating methods offer better temperature control by using the battery's own resistance, though they are harder to manage and still under experimental study [20].

Research developed at the vehicle level has been focused on boosting thermal efficiency, and as such, it has led to the development of Integrated Thermal Management Systems (ITMS) [21]. This system utilizes waste heat from both the engine and motor, employing heat exchangers and a heat pump. This design achieved up to a 55.94% reduction in battery warm-up time, a 27.39% improvement in thermal efficiency, and a 5.18% decrease in overall energy usage [21].

Recent research has also introduced as an advanced method the hybrid heating strategies that combine both internal and external mechanisms [22]. Lastly, regarding safety, [22] presented a control strategy using a multi-objective genetic algorithm, optimizing the trade-off between warm-up duration and capacity loss to enable flexible thermal management across varying environmental conditions.

Currently, air and liquid-based heating methods are the most widely adopted in commercial EVs such as those produced by Toyota and Tesla [14], [20], [23], with external heating being particularly common in recent models equipped with NCM batteries. For instance, from 2020 to 2023, models such

as the Tesla Model Y (60 kWh), Volkswagen ID.4 CROZZ (84.8 kWh), Audi Q5 e-tron (83.4 kWh), and XPeng P7 (86.2 kWh) all adopted external heating strategies using the liquid coolant to manage battery temperature [24]. These cases reflect the continued preference for external heating in supporting thermal performance. Despite their prevalence, these methods are energy-intensive and can result in low overall system efficiency [14] [23]. Furthermore, research has focused on the use of phase change materials (PCM) which have shown promise by enabling rapid preheating through the Joule heating effect. However, these systems often rely on an external electrical source to generate the required heat, which may affect their practicality [14].

2.3 Simulation and Modeling Techniques

One-dimensional (1D) simulations have been effectively employed to analyze the thermal response of lithium-ion batteries, particularly under extreme operating conditions [25]. Although their use is somewhat limited, 1D models remain valuable due to their lower computational cost and ability to capture key trends.

For example, [26] developed a 1D lithium-ion battery model in COMSOL Multiphysics by coupling a pseudo two-dimensional electrochemical model with a thermal model to evaluate the impact of thermal boundary conditions. These included isothermal, adiabatic, and convective cooling with heat transfer coefficients ranging from 0.1 to 10 W/m²·K. Their findings showed that boundary conditions have a strong influence on the thermal behavior of the cell. Similarly, [27] used a 1D isothermal model in COMSOL to assess battery performance at different C-rates, showing that higher discharge rates up to 3C led to greater internal voltage gradients.

While AVL CRUISE™ M is less represented in academic battery literature, it is widely used in industry for simulating complex interconnected vehicle systems. The strength of the software lies in its modular architecture, which allows the coupling of subsystems such as powertrains, thermal management, and batteries as demonstrated by [28], who focused on dynamic vehicle simulations. Lastly, AVL CRUISE™ M has been applied to extract charging profiles and support battery cell optimization, demonstrating its potential for electrochemical and thermal co-simulation [29].

As a simplified modeling technique for evaluating the thermal behavior of a lithium-ion battery module, a global energy balance, presented by [22], can be applied to estimate the temperature evolution over time using equation (1).

$$C_p \cdot m \cdot \frac{dT}{dt} = I^2 \cdot R + I \cdot T_{amb} \frac{dU_{ocv}}{dT} - \dot{Q}_{coolant} - h \cdot A \cdot (T - T_{amb}) \quad (1)$$

This expression accounts for the main contributors to heat generation and dissipation during battery operation. The left-hand side represents the thermal inertia of the system, where C_p is the specific heat capacity, m is the mass of the module, and $\frac{dT}{dt}$ is the rate of temperature change. On the right-hand side, $I^2 \cdot R$ corresponds to irreversible ohmic heating, while the term $I \cdot T_{amb} \frac{dU_{ocv}}{dT}$ captures the entropic heat associated with the electrochemical reactions, while heat removal is represented by two terms: $\dot{Q}_{coolant}$, accounting for active cooling, and $h \cdot A \cdot (T - T_{amb})$, representing convective heat losses to the surrounding environment, where h is the convective heat transfer coefficient and A is the heat exchange surface area [22].

This simplified approach enables an efficient estimation of temperature dynamics in battery systems without requiring detailed multiphysics simulations, making it well-suited for system-level studies or control-oriented modeling.

2.4 Gaps in Current Research

Despite progress in lithium-ion battery thermal management, several gaps remain in current research. First, although thermal management of lithium-ion batteries has been extensively investigated, limited attention has been paid to how different arrangement designs specifically impact the thermal behavior of 21700-format cells [30].

While low-temperature heating during discharge has been shown to improve battery temperature and performance, there is a need for further research on how to control this heating without introducing safety risks. Excessive heat, as noted in [31], may compromise reliability and increase the likelihood of thermal events.

Finally, although various heating methods have proven effective at the individual cell level, there is a clear lack of studies that address the scalability of these solutions to the module or pack level [22]. Research in [23] emphasizes the importance of bridging this gap to enable practical integration into real systems.

Despite the popularity of research on lithium-ion batteries, as presented by [32], there is still a need to address one of their most well-known challenges: their reduced performance at sub-zero temperatures, which continues to limit the broader adoption of EVs.

Chapter 3

Cell Characterization and Thermal Behavior at Low Temperatures

3.1 Introduction

To evaluate the necessity of a heating system in a battery module, it is important to understand the behavior of 21700 lithium-ion battery cells under different temperature conditions. Several testing methods are available for this purpose. However, the static capacity test was selected in this study due to its non-invasive, straightforward and reliable procedure, as supported by [33]. This approach enabled a clear observation of the cell's thermal behavior under controlled and steady conditions.

Experimental capacity tests were carried out at a constant discharge rate to replicate cold start conditions. The objective was to observe the thermal behavior of the cell under various ambient temperatures, focusing on tracking voltage, capacity and surface temperature changes over time. Following this, simulations were conducted using the same test conditions to complement the experimental results. These allowed exploration of additional scenarios that were not feasible to test physically. Therefore, as a final step, simulations under adiabatic conditions were performed to isolate the cell's internal heat generation and examine its theoretical thermal response under a perfectly insulated condition without external heat losses.

The results aim to provide a practical perspective on the cell's thermal behavior under realistic operating conditions, offering a preliminary understanding of how it responds to cold temperatures. These insights help anticipate the cell's standalone thermal performance and lay the groundwork for future module-level design considerations.

3.2 Experimental Methodology

3.2.1 Test Setup

The cell selected for this study was the 21700 INR Samsung lithium-ion cell, commonly used battery applications. Table 1 summarizes their key specifications relevant to the experimental capacity test conducted from [34].

Table 1. 21700 Battery Cell Specifications

Category	Specification Items	21700-50E2
General	Typical Capacity (4.2V, 0.2C discharge, mAh)	5000
	Nominal Voltage (V)	3.63
Charge	Charging Voltage (V)	4.2
Discharge	Discharging End Voltage (V)	2.5
	Standard Discharging Current	0.2C
	Max Discharging Current (not for continuous)	3.0C (14.7A)

The static capacity test was performed using a battery cycler and a thermal chamber as presented in Figure 1. The MACCOR battery cycler model 4200 was used to control the charge and discharge profiles of the cell and record the voltage, current and time data. The CSZ Sub-Zero MicroClimate thermal chamber was used to ensure a controlled temperature environment during testing. Lastly, the temperature measurements were obtained using thermocouples. Data acquisition was managed by DAQNavii Data Logger Software from the Advantech USB – 4718 thermocouple input module.

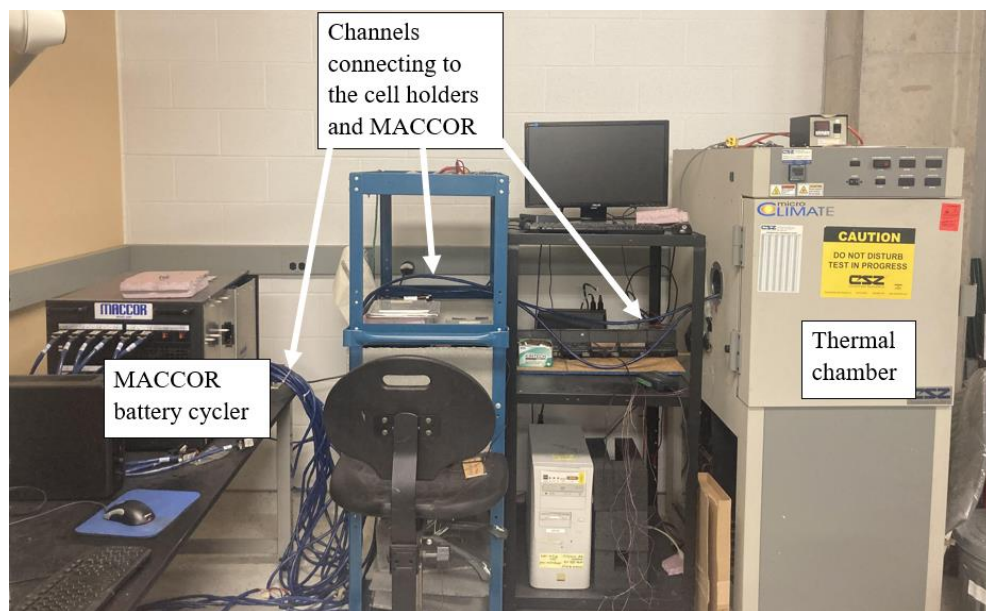


Figure 1. Experimental setup for battery cell testing

To perform the test, the cell was placed inside the thermal chamber and secured in a 21700 cell holder as shown in Figure 2, which kept it fixed throughout the test. The holder was connected to the MACCOR battery cycler via two cables attached to each terminal, enabling control and data acquisition. A thermocouple was affixed to the center of the cell to monitor surface temperature and connected to the Advantech USB-4718 module for temperature data logging.

During testing, the cell was positioned horizontally on fire-resistant insulation foam, providing stability and preventing contact with conductive surfaces as shown in Figure 2.

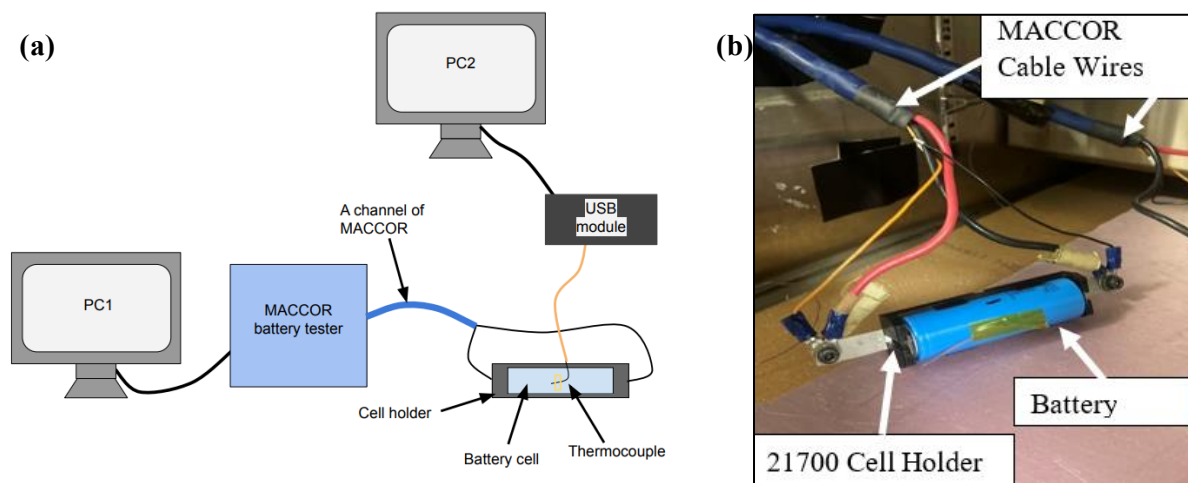


Figure 2. Device under test a) Overview of the test connections b) Cell set up

3.2.2 Test Procedure

The static capacity test procedure consisted of a series of controlled steps adapted from [35]. The procedure sequence, presented in Figure 3, included cell preparation using a constant current constant voltage (CCCV) charging, then a resting period followed by the constant current discharge ending in a rest period. In specific, the cell was placed in the thermal chamber set to 30 °C and left for 30 minutes to allow for temperature stabilization at open circuit voltage. Then, the cell was charged at constant current $C/2$ (2.5 A) until reaching max voltage (4.2 V). Subsequently, the cell was charged at constant voltage (4.2 V) until the current dropped to $C/20$ (0.254 A). After charging, the thermal chamber was adjusted to the chosen test temperature, and the cell was rested at open circuit voltage for 1 hour to ensure thermal equilibrium. Afterwards, the cell was discharged at constant current $1C$ (4.9 Ah) until min voltage was reached (2.5 V) at different ambient temperatures. Lastly, the cell was rested for 1

hour at open circuit voltage and ambient temperature to allow voltage stabilization. To ensure safe storage, the cell was charged at C/2 for 30 minutes to reach approximately 50% SOC (3.7 V).

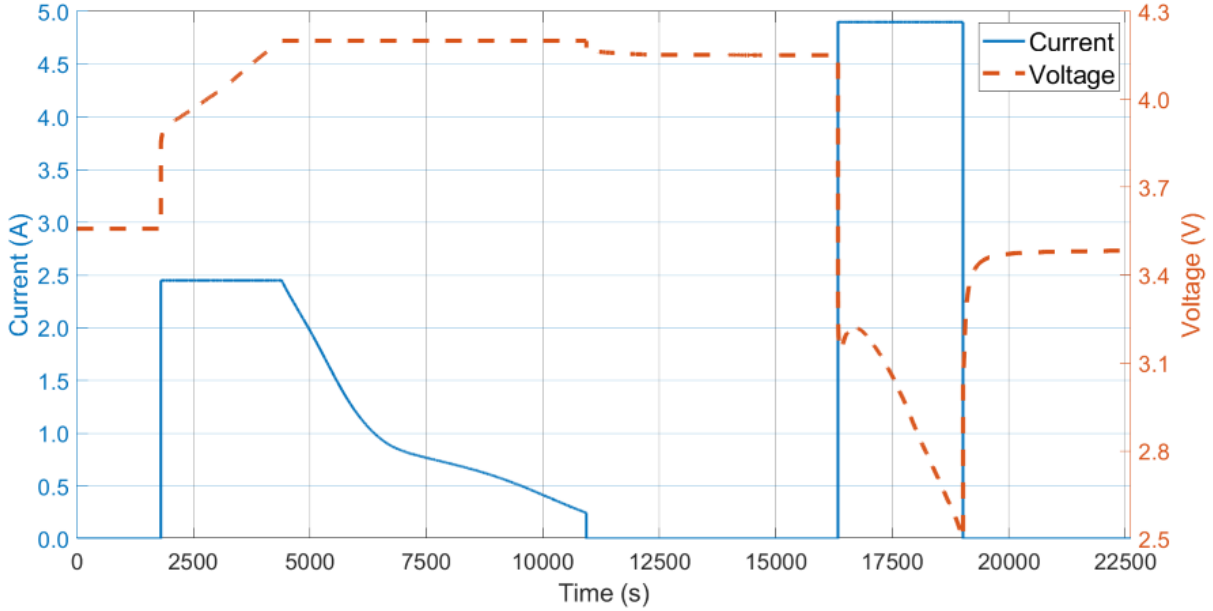


Figure 3. Current and voltage profiles of the capacity test applied to the 21700 lithium-ion cell

The testing conditions included four ambient temperatures: -12°C , -3°C , 11°C and 30°C . These temperatures span from sub-zero to warm environments. Although the manufacturer allows discharge down to -20°C [34], the lowest temperature used in this study was -12°C to ensure both safe operation and practical test execution. This range still captures key sub-zero behavior while maintaining experimental feasibility. All tests were conducted at a constant 1C discharge rate, representing a moderate yet realistic load condition. The detailed test sequence programmed into the equipment is provided in Appendix A.

3.3 Simulation methodology

3.3.1 Model configuration overview

Thermal system simulations were developed to replicate the discharge behavior of the Samsung 21700 lithium-ion battery cell under controlled conditions. The objective was to analyze how cold start conditions, characterized by low initial temperatures, influence the temperature rise during discharge. The simulation model used the Batemo GmbH I model in a Functional Mock-up Unit (FMU), which provides the electrochemical-thermal battery model of the Samsung 21700 lithium-ion battery cell.

AVL CRUISE™ M software was used to run simulations reflecting the system-level interconnections. A constant current source was applied to the battery cell to simulate a 1C discharge rate, matching the conditions used in the experimental methodology. The electrical circuit is completed with an electric node and ground reference point. The simulation outputs considered were voltage, cell capacity and surface temperature (T_s) to allow for comparison with the experimental data.

Two simulation scenarios were developed to analyze the thermal behavior of the battery cell: one representing convection and the other simulating with adiabatic conditions.

3.3.2 Discharge simulation with a convective thermal model

In the first scenario, heat exchange with the environment was modeled by coupling the battery cell to a convection block. This configuration enabled the simulation of natural convective conditions that allowed the heat generated during discharge to dissipate into the surroundings. A convective heat transfer coefficient of $20 \text{ W/m}^2\text{K}$, as established by [17] to represent natural convection at the battery surface, was used as a boundary condition, along with ambient temperatures matching those in the experimental tests, and a heat transfer area of 5311 mm^2 , corresponding to the exposed surfaces of the cell. The simulation setup is shown in Figure 4.

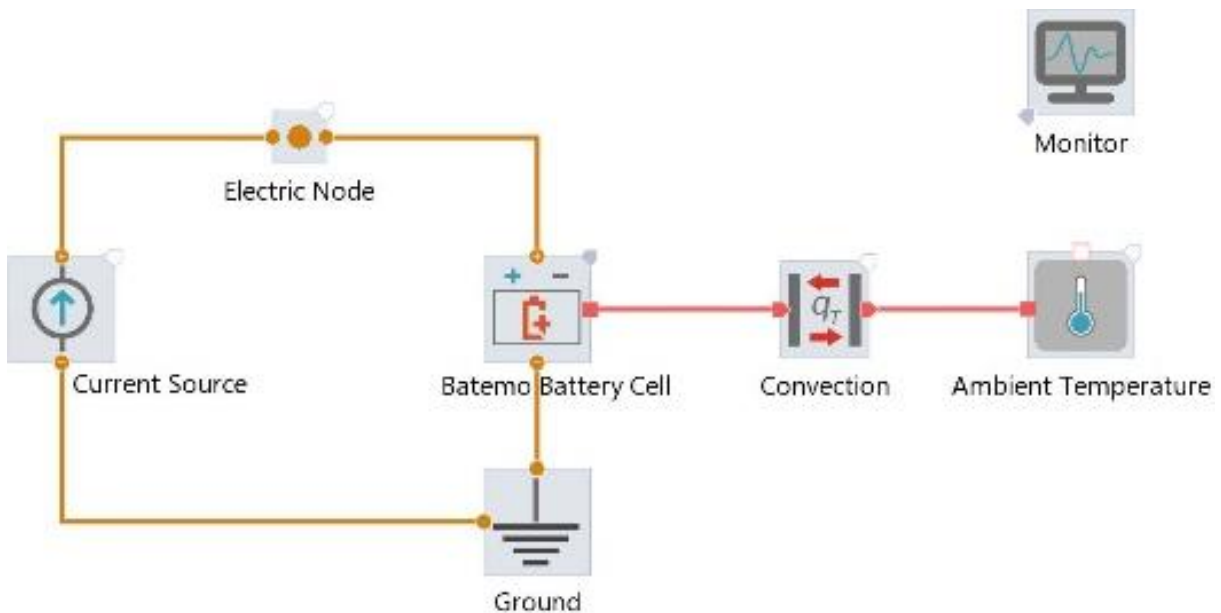


Figure 4. Configuration of the battery cell discharge simulation setup under convective conditions

3.3.3 Discharge simulation under adiabatic conditions.

In the second case, the simulation was performed under adiabatic conditions to isolate the effect of internal heat accumulation and eliminate external thermal influence. In this model, the thermal connection to the environment was removed which allowed the internal temperature to rise because of the battery discharge.

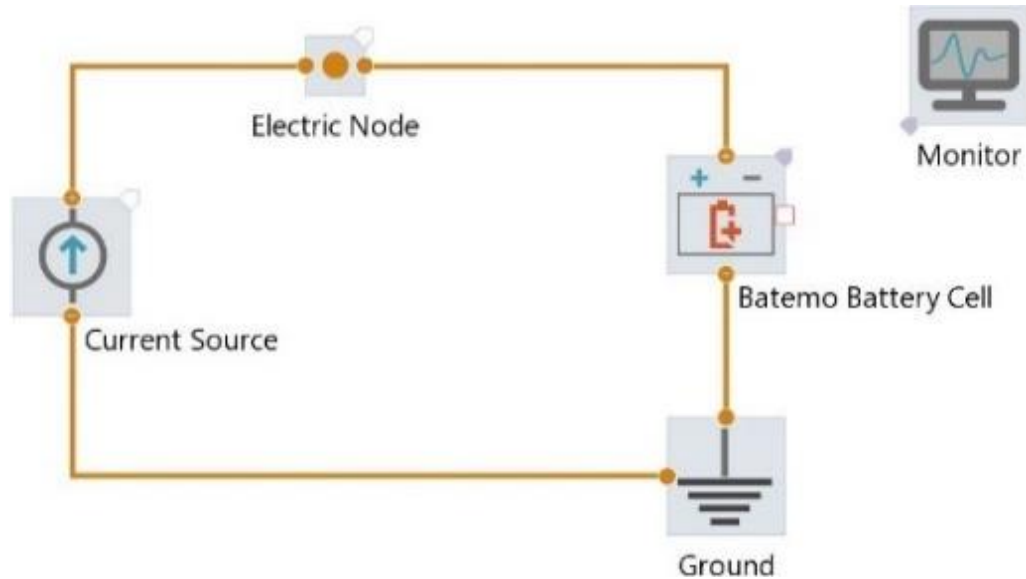


Figure 5. Configuration of the battery cell discharge simulation setup under adiabatic conditions

3.4 Results

3.4.1 Capacity Behavior at Cold Temperatures

To explore the limitations of lithium-ion batteries under cold start conditions, discharge curves were obtained at different ambient temperatures. These curves illustrate how the cell's capacity changes in relation to voltage, highlighting the impact of temperature on performance. Figure 6 shows the relationship between voltage and capacity for the different set ups.

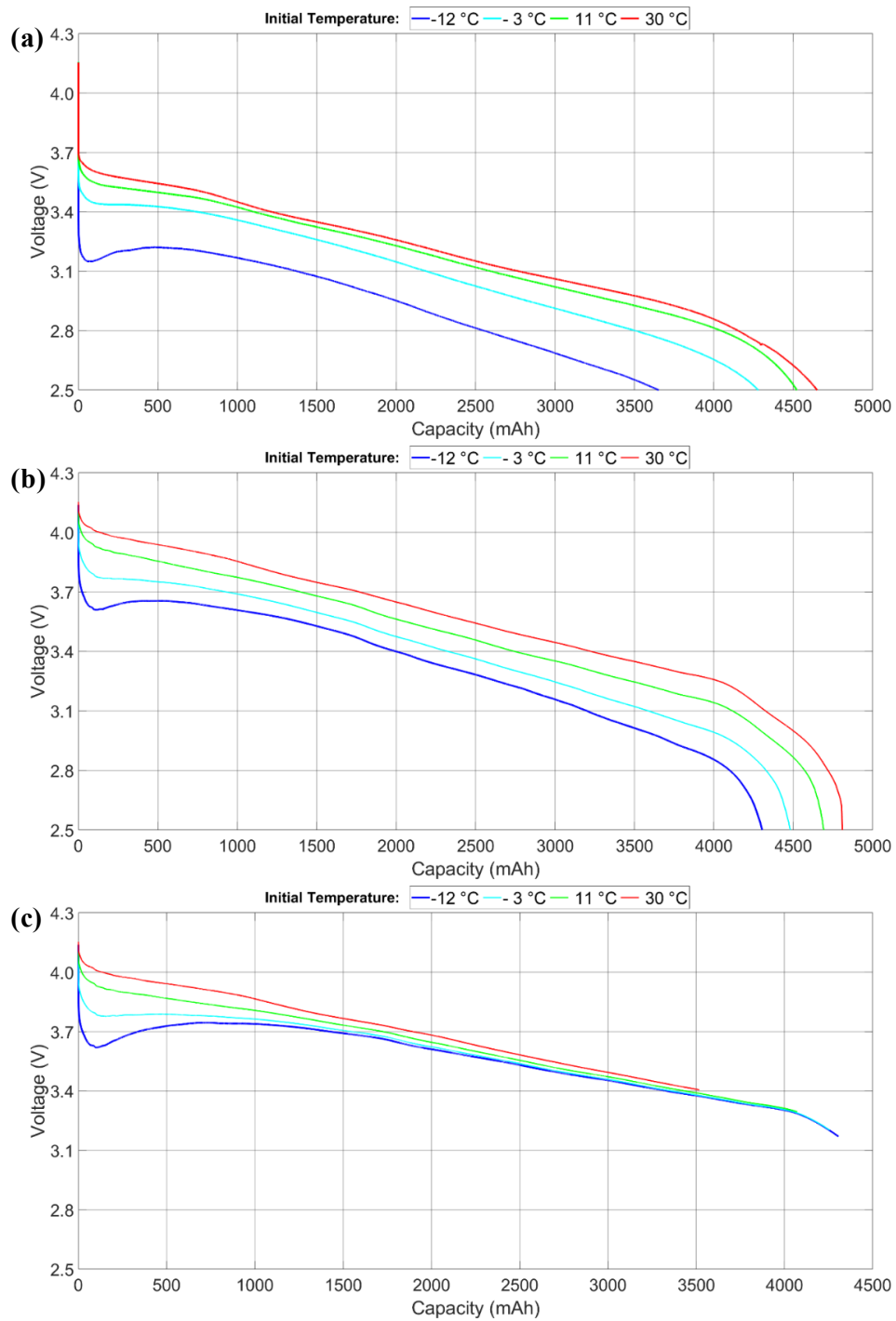


Figure 6. Discharge curves of a 21700 lithium-ion cell at different ambient temperatures for (a) experimental results, (b) simulations under convective conditions, and (c) simulations under adiabatic conditions, all at a 1C discharge rate (4.9 A).

The discharge curves show different results comparing the experimental and simulated results. The experimental curves demonstrate similar effect of temperature on lithium-ion performance with the literature: lower temperatures reduce capacity and increase resistance, as evidenced by the reduced delivered capacity and pronounced initial voltage drops. The distinct behavior at $-12\text{ }^{\circ}\text{C}$, where the voltage briefly recovers after an early dip, could reflect transient internal heating during discharge that momentarily improves conductivity before continued energy draw resumes the voltage decline.

In contrast, simulations under convective conditions show smoother and higher discharge curves across all temperatures. This could stem from idealized thermal coupling or the absence of extra losses such as the contact resistance with the components of the testing set up. Moreover, the experimental curves show a more pronounced initial voltage drop than the simulated ones under convective conditions. As presented in [36], this drop could be associated with an increase in linear ohmic resistance. Therefore, additional resistance contributions from the experimental setup, such as contact points, wiring, or connectors, may have further amplified this effect. Lastly, the discrepancy between experiment and simulation results might be also related to the choice of convective heat transfer coefficient of $20\text{ W/m}^2\text{K}$, as a more accurate value would have improved the representation of heat exchange with the environment.

In the case of the adiabatic simulation, the thermal losses are removed completely. Thus, the effect of internal heating becomes dominant. Despite starting at low temperatures, all discharge curves converge toward the high temperature performance by the end of the cycle. This indicates that internal heat generation during discharge is sufficient to raise the cell temperature significantly (which will be shown in the next section), improving kinetics and reducing resistance over time. Furthermore, this result is consistent with the findings of [26], who showed that discharge capacity improves under thermally insulated conditions. Lastly, this result highlights a key trade-off in battery design. While insulated conditions in simulations improve capacity by retaining heat and allowing the cell to warm during discharge, real systems must prioritize safety by limiting temperature rise.

To further analyze the discharge behavior, [37] illustrates an Open Circuit Voltage (OCV) vs SOC curve segmented into three zones based on the SOC. It highlights three distinct zones. The first zone shows an exponential voltage drop above 70% SOC, mainly due to ohmic resistance. The second zone, from 70% to 25%, is nearly linear, reflecting optimal cell kinetics. In the third zone, a sharp decline near full discharge arises from diffusion limitations and polarization. Although the OCV curve

represents ideal, no-load behavior, the tested 1C discharge curves follow a similar trend, with the same characteristic zones. The main difference lies in the added voltage drop due to internal resistance and dynamic effects.

To support the analysis and provide an additional point of comparison, a first-order equivalent circuit model (ECM) was implemented using parameter values from the literature as a reference. This ECM captures key electrochemical dynamics of a 21700 lithium-ion cell during constant current discharge through open-circuit voltage (OCV), a series ohmic resistance (R_0), and a parallel RC network consisting of a polarization resistance (R_1) and (C_1). To produce the voltage vs SOC curves considering the reference ECM equations (2), (3), (4) were used to determine terminal voltage, RC branch voltage and SOC, respectively.

$$V_{(k)} = V_{ocv}(k) - I \cdot R_0 - V_{RC}(k) \quad (2)$$

$$V_{RC}(k) = \frac{V_{rc}(k-1) + \frac{\Delta t \cdot I}{C_1}}{1 + \frac{\Delta t}{R_1 \cdot C_1}} \quad (3)$$

$$SOC_k = SOC_{k-1} - \frac{\Delta t}{3600} \quad (4)$$

The selected parameter values: $R_0 = 0.0265 \Omega$, $R_1 = 0.016 \Omega$ and $C_1 = 0.036 \text{ F}$ were taken from [38], based on prior experimental characterization of this specific cell type. The OCV at each time step is interpolated from a lookup table as a function of the SOC, with the full OCV–SOC profile provided in Appendix B. This literature-based ECM was used as an independent reference to compare both the experimental results and the thermal system simulation electrothermal simulations developed in this study, helping to further validate and contextualize observed discrepancies.

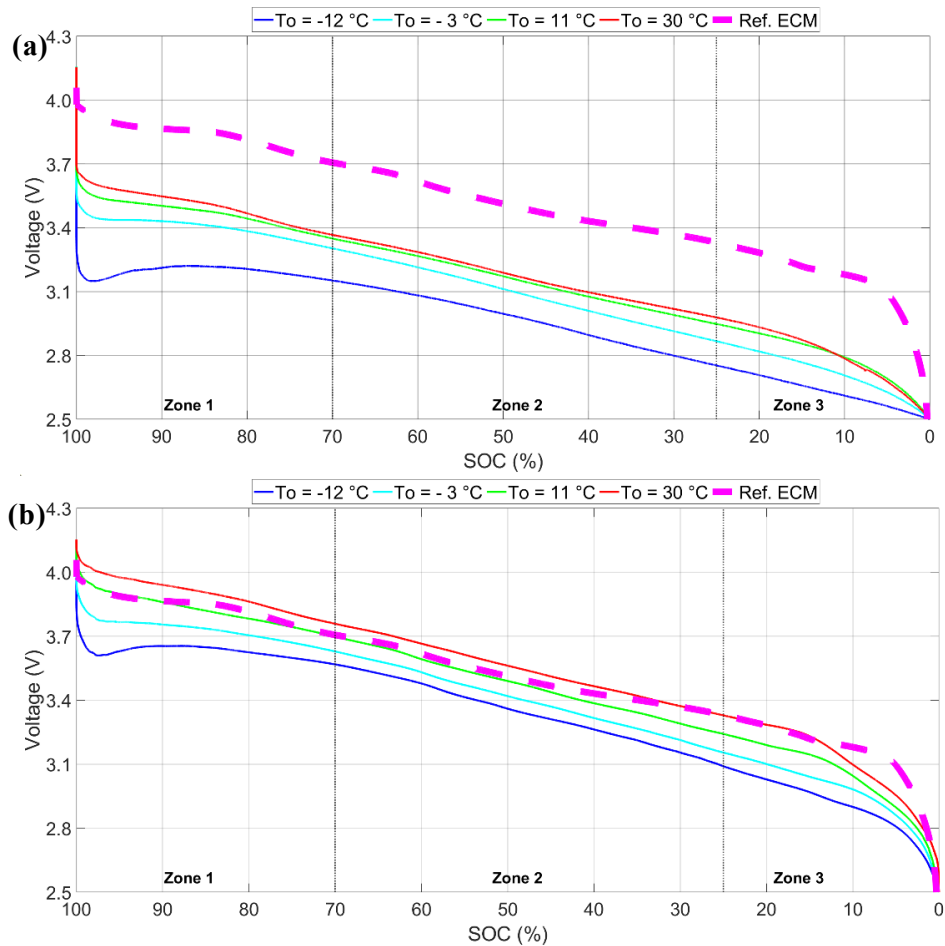


Figure 7. Discharge voltage curves of a 21700 lithium-ion cell at different ambient temperatures, segmented by SOC zones and compared with the reference ECM for (a) experimental results and (b) simulations under convective conditions.

The discharge voltage curves segmented by SOC zones reveal distinct behaviors across experimental, simulated, and ECM reference data. In Zone 1 (100–70% SOC), the experimental curves show a steep voltage drop, especially at sub-zero temperatures, due to increased ohmic resistance. The simulated curves and ECM curve follow the same trend but with a smoother decline, underestimating real-world transients. The ECM reference remains nearly flat in this region, overpredicting voltage and failing to capture temperature effects as parameters are generally estimated at 25 °C. In Zone 2 (70–25% SOC), all curves exhibit a more linear and stable decline, representing optimal reaction kinetics. Here, the convective simulation aligns more closely with the ECM, considering this zone allows for linear conditions. Finally, Zone 3 (below 25% SOC) is marked by a sharp voltage drop as the cell approaches

full discharge, driven by diffusion limitations. The reference ECM and simulated convection present a higher voltage drop compared with the experimental results. Overall, the ECM and simulated convection results follow the experimental trends but overestimate the voltage response, likely due to limited thermal sensitivity. In contrast, extra resistance from contact points, wiring, or connectors in the experimental setup may have caused a larger voltage drop, leading to lower measured values not captured in the simulations.

Table 2 presents the capacity obtained after a complete discharge at 1C that corroborates the trends presented in the figures presented previously. The capacity loss was calculated relative to the 30 °C experimental baseline using equation (5).

$$\text{Capacity loss} = \left(1 - \frac{C_T}{C_{30^\circ\text{C}}}\right) \times 100 \quad (5)$$

Where C_T is the capacity at a given ambient temperature and $C_{30^\circ\text{C}}$ is the reference capacity at 30 °C. To assess model accuracy, the capacity error, presented in equation (6) was defined as the difference between experimental and convective simulation results.

$$\text{Capacity error} = \left| \frac{C_{sim} - C_{exp}}{C_{exp}} \right| \times 100 \quad (6)$$

Table 2. Capacity results of a 21700 li-ion cell discharged at 1C rate (4.9 A) at different ambient temperatures

Ambient temperature (°C)	Experimental capacity (mAh)	Simulation capacity - convection (mAh)	Simulation capacity - adiabatic (mAh)	Experimental capacity loss (%)	Convective simulation capacity loss (%)	Capacity error (%)
-12	3652	4304	4306	21	11	16
-3	4279	4481	4257	8	8	4
11	4522	4692	4072	3	3	3
30	4650	4809	3517	-	-	3

The influence of ambient temperature on discharge capacity is presented in both the experimental data and the convection-based simulations. As temperature decreases, capacity loss increases, reaching 21% at -12 °C in the experimental case. The convection-based simulation results follow the trend but may underestimate losses in extreme cold, showing a decrease of only 11%. Lastly, at -3 °C and 11 °C, both

the experimental and simulated results show similar losses of 8% and 3% respectively. On the other hand, in the adiabatic simulation, capacity appears to drop as temperature increases. However, this is not due to actual performance degradation but because the cell reached the maximum temperature limit, stopping the simulation. As such, the adiabatic case should be used to assess how the surface temperature evolves over time, rather than to predict actual capacity.

To further examine how temperature influences battery behavior, the OCV at the beginning of discharge was compared between experimental data and simulation results. The OCV error was calculated using equation (7).

$$OCV\ Error = \left| \frac{V_{sim} - V_{exp}}{V_{exp}} \right| \times 100 \quad (7)$$

Where V_{sim} refers to the simulated OCV (under convective conditions) and V_{exp} to the experimental measurement. The results are summarized in Table 3

Table 3. OCV results of a 21700 Li-ion cell discharged at 1C rate (4.9 A) at different ambient temperatures

Ambient temperature (°C)	Experimental OCV (V)	Simulation convection OCV (V)	Simulation adiabatic OCV (V)	OCV error (convective) (%)
-12	4.151	4.138	4.138	0.30
-3	4.157	4.144	4.144	0.30
11	4.156	4.149	4.149	0.20
30	4.154	4.153	4.153	0.00

The simulated OCV values show strong agreement with experimental data across all temperatures, with a maximum error of just 0.30%. Moreover, the variation in OCV is minimal, indicating that ambient temperature has little influence on the OCV prior to discharge.

To analyze the effect of ambient temperature on the cell's early dynamic response, the initial loaded voltage, defined as the voltage measured at the first data point under load, was explored under various thermal conditions. The initial loaded voltage loss was then calculated to quantify the reduction in voltage compared to the 30 °C reference case, using the equation (8).

$$\text{Initial loaded voltage loss} = \left(1 - \frac{V_T}{V_{30^\circ\text{C}}}\right) \times 10 \quad (8)$$

Where V_T is the initial loaded voltage at a given ambient temperature, and $V_{30^\circ\text{C}}$ is the value at 30°C . The results are summarized in Table 4.

Table 4. Initial voltage drop of a 21700 Li-ion cell discharged at 1C rate (4.9 A) at different ambient temperatures

Ambient temperature (°C)	Experimental initial loaded voltage (V)	Simulation convection initial loaded voltage (V)	Simulation adiabatic initial loaded voltage (V)	Experimental initial loaded voltage loss (%)	Simulation initial loaded voltage loss (%)
-12	3.363	3.795	3.845	9	8
-3	3.589	3.966	3.996	3	4
11	3.677	4.068	4.068	1	1
30	3.699	4.113	4.113	-	-

The experimental results show a clear influence of ambient temperature on the cell's voltage response at the start of discharge. At lower temperatures, the cell exhibits a more pronounced voltage drop, reaching 9% below the baseline at -12°C . As the temperature increases, improved ion mobility and faster reaction kinetics reduce internal resistance, resulting in a smaller voltage loss, as low as 1% at 11°C . This trend is consistently captured by simulations under both convective and adiabatic conditions. While both models mostly predict similar behavior, a slight difference appears at -12°C , where the adiabatic case shows a smaller voltage drop. In this case, the absence of heat loss to the environment may have allowed the cell to retain more of its internally generated heat, which helped reduce internal resistance.

3.4.2 Thermal Response at Cold Start Conditions

A comparative view of the surface temperature change during discharge is shown in Figure 8 illustrating how different initial temperatures influence the cell's thermal response.

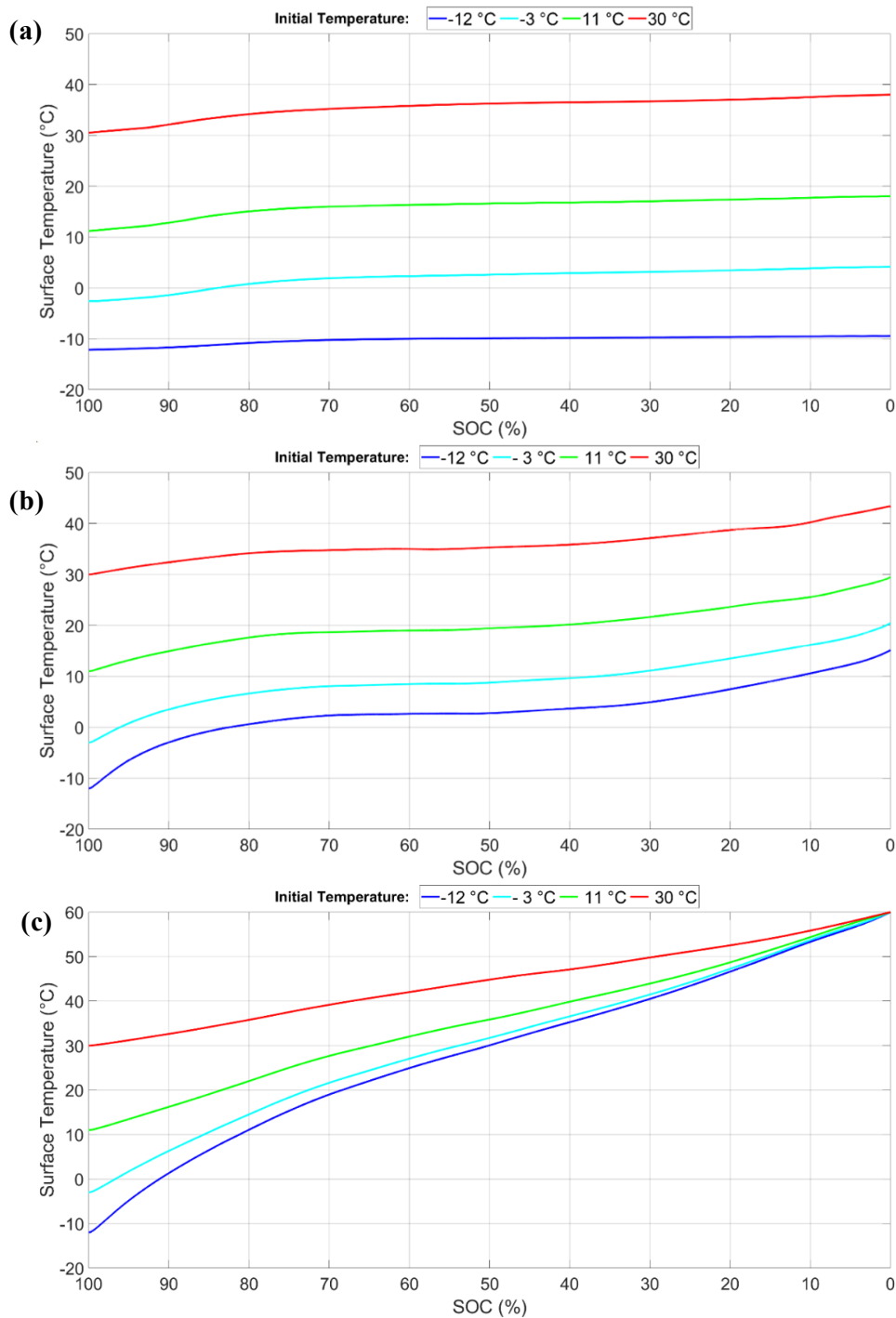


Figure 8. Surface temperature plots of a 21700 lithium-ion cell as a function of SOC for (a) experimental data, (b) simulation with convective conditions, and (c) simulations under adiabatic conditions, at -12 °C, -3 °C, 11 °C, and 30 °C and at 1C discharge rate (4.9 A).

The overall trend is consistent: higher initial ambient temperatures result in higher surface temperatures throughout the discharge. This is expected, as at warmer starting conditions the cell requires less energy to overcome thermal resistance, and electrochemical reactions proceed more efficiently, generating more internal heat (Source).

In the experimental results, the temperature rise is modest, especially at lower initial temperatures. At -12 °C, the curve remains nearly flat, indicating minimal temperature change, while at 30 °C, the increase is more gradual but consistent. This suggests that ohmic and charge transfer resistances remain high, limiting current and internal heat generation. On the other hand, in the convective simulation, the trends are more pronounced. Each curve shows a steeper and more continuous rise in temperature compared to the experimental case. This change might be produced because under convective assumptions, internal heating becomes more dominant as discharge progresses. Lastly, the adiabatic simulation shows the most significant differences. All curves display a nearly linear and steep increase in temperature with SOC reduction, and the gap between initial temperatures narrows toward the end of discharge. The convergence of all curves at the end suggests that the thermal effect of starting temperature is overtaken by internal heating.

To complement the previous plots, Table 5 presents the final surface temperatures reached by the cell under each thermal condition.

Table 5. Final surface temperature of a 21700 Li-ion cell discharged at 1C rate (4.9 A) at different ambient temperatures

Ambient temperature (°C)	Experimental Final temperature (°C)	Simulation convection final temperature (°C)	Simulation adiabatic final temperature (°C)
-12	-10	12	58
-3	3	20	59
11	18	30	60
30	38	43	60

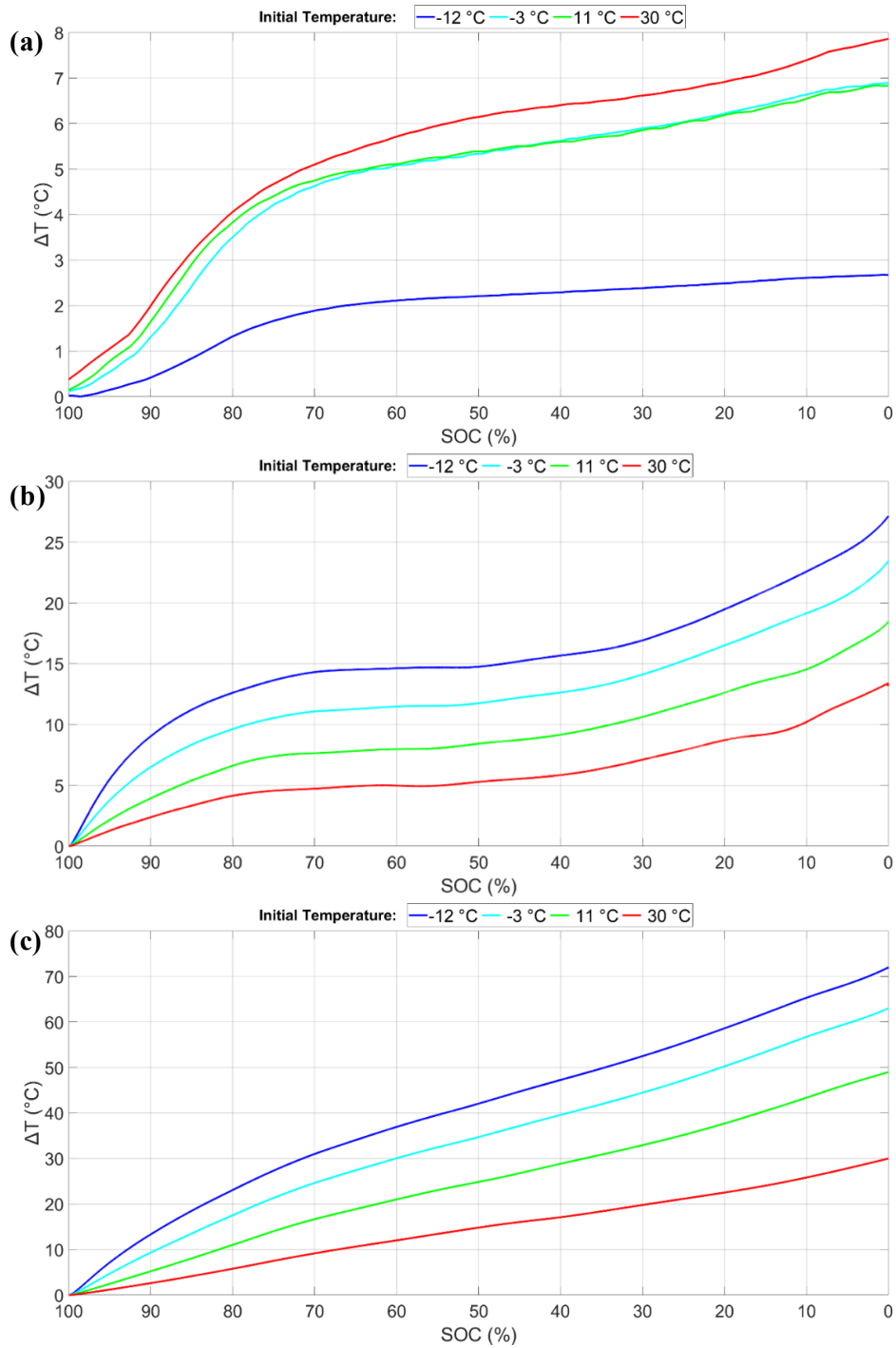


Figure 9. Surface temperature rise (ΔT) of a 21700 lithium-ion cell as a function of SOC for (a) experimental results, (b) simulations with convective conditions, and (c) simulations under adiabatic conditions, at -12 $^{\circ}\text{C}$, -3 $^{\circ}\text{C}$, 11 $^{\circ}\text{C}$, and 30 $^{\circ}\text{C}$ under a 1C discharge rate (4.9 A)

The temperature rise differs considering the test. In the experimental results, ΔT increases moderately during discharge, with the highest rise observed at 30 °C and the lowest at -12 °C.

The curves begin to plateau after around 60% SOC, indicating that more heat is lost to the environment as the cell warms. Notably, the spacing between curves is narrow, especially between -3 °C and 11 °C, suggesting that the environmental heat loss is dominant and somewhat dampens the effect of the initial temperature on net heat retention.

Moreover, considering the convective simulation, the ΔT values are significantly higher than in the experimental case, particularly at lower initial temperatures. Also, the curves show a steeper increase with SOC reduction and a stronger separation between temperature levels. Remarkably, the trend reverses compared to the experimental case: the greatest ΔT occurs at -12 °C. This result might suggest that the heat generated is partially retained. Thus, at colder starting temperatures, the thermal gradient between the cell and the surroundings is larger, initially leading to higher heat loss, but then progressively allowing more heat to accumulate as the discharge progresses. This results in a sharper ΔT rise toward lower SOC.

Lastly, in the adiabatic simulation, the temperature rise is dramatically higher across all conditions. ΔT increases almost linearly with SOC reduction. The curves are clearly separated, with the largest ΔT occurring at -12 °C and the smallest at 30 °C. This inversion in the results compared to the experimental case, highlights that in adiabatic conditions, colder starts result in more internal resistance and thus more heat generation, and with no heat losses, all that energy accumulates within the cell.

Overall, these results underline how boundary conditions shape thermal behavior. In experiments, external heat loss limits temperature rise, while in simulations, particularly adiabatic ones, internal heating dominates. The reversed trends between experimental and simulated data emphasize the role of heat dissipation in real systems.

Table 6 presents the influence of thermal boundary conditions on cell heating summarizing the total surface temperature rise observed experimentally and in both simulation scenarios.

Table 6. Comparison of surface temperature rise (ΔT) between experimental results and simulations under convective (Case C) and adiabatic (Case A) conditions for different initial ambient temperatures.

Initial temperature (°C)	Experimental ΔT (°C)	Simulation Case convection ΔT (°C)	Simulation Case adiabatic ΔT (°C)	Ratio (Adiabatic ΔT / convection ΔT)
-12	2.7	24	71	2.9
-3	6.8	23	62	2.7
11	6.7	18	50	2.6
30	7.9	13	30	2.3

The table reveals a clear divergence in temperature rise depending on the thermal boundary condition applied. In the experimental results, the surface temperature rise (ΔT) remains below 8 °C across all conditions, showing minimal self-heating due to significant heat losses to the environment. In contrast, the convective simulation (Case C) predicts substantially higher temperature rises at colder ambient temperatures, with ΔT reaching 24 °C at -12 °C and decreasing as the ambient temperature increases.

This inverted trend suggests that under partial insulation, colder stars lead to greater internal heat generation due to higher internal resistance, and a portion of that heat is retained, allowing more warming during discharge. Moreover, the adiabatic case (Case A) further amplifies this trend, with ΔT rising to 71 °C at -12 °C and dropping steadily to 30 °C. Since no heat is lost in this scenario, the temperature rise directly reflects internal heat generation. The large ΔT at colder temperatures indicates that while initial performance is limited, the heat accumulates significantly, allowing the cell to recover performance mid-discharge. Overall, this table emphasizes how heat retention mechanisms drastically influence thermal behavior.

3.5 Summary of Findings

Chapter 3 highlights the critical role of thermal boundary conditions on the temperature behavior and discharge performance of a 21700 lithium-ion cell under cold-start scenarios. Regarding the discharge voltage and capacity behavior, experimentally at -12 °C, the cell delivered under 3652 mAh, compared to over 4650 mAh at 30 °C. Voltage dropped more steeply at lower temperatures. The experimental setup likely included extra resistance from wiring and contacts, contributing to lower measured

voltages. In contrast, simulated convection results followed the overall trend but overestimated voltage, likely due to limited thermal sensitivity and the absence of parasitic resistances.

Building on this, the SOC segmented analysis showed Zone 1 with an initial voltage drop, Zone 2 with a gradual decline, and Zone 3 with a sharp drop. While simulations and the ECM model captured this general trend, they consistently overpredicted voltages. This discrepancy is likely due to both the simplified thermal behavior in models and experimental error sources, such as contact resistance and instrumentation inaccuracy.

As for the surface temperature evolution, there is a clear contrast between experimental and simulated temperature profiles. Experimentally, the surface temperature rose modestly, reaching just $-10\text{ }^{\circ}\text{C}$ at $-12\text{ }^{\circ}\text{C}$ and up to $38\text{ }^{\circ}\text{C}$ at $30\text{ }^{\circ}\text{C}$. In contrast, simulations under convective boundary conditions predicted a much steeper rise, reaching $12\text{ }^{\circ}\text{C}$ at $-12\text{ }^{\circ}\text{C}$. Adiabatic conditions produced the most extreme case, with a ΔT of up to $71\text{ }^{\circ}\text{C}$ under the same cold start. This reveals a reversal in trend: under experimental conditions, higher ambient temperatures led to more warming, while simulations predicted greater self-heating at lower temperatures due to increased resistive losses. This highlights the influence of external thermal dissipation, which limits actual temperature rise despite high internal heat generation.

Moreover, the temperature rise (ΔT) relative to ambient further demonstrates the divergence between real and simulated environments. In experiments, ΔT remained relatively low throughout discharge, especially at colder temperatures. This suggests effective heat exchange with the surroundings. On the other hand, simulations, especially under adiabatic assumptions, showed a steady increase in ΔT , with no external heat loss to temper the rise. These results demonstrate that while the cell can indeed self-warm through internal losses, the magnitude of temperature rise is governed predominantly by the surrounding thermal conditions. Accurate modeling of these boundaries is essential for predicting cold-start behavior.

Chapter 4

Conceptual Module Design Basis for Thermal Simulation

4.1 Introduction

Below zero temperature operation leads to a reduction in cell capacity, highlighting the need for heating strategies. While several methods to enhance the thermal performance of batteries at the cell level have been developed, their implementation becomes impractical when scaled to module level due to the increased complexity of managing large groups of cells. Instead, solutions at module level, like existing cooling strategies, might offer a practical approach. To study the effectiveness of heating strategies at module level, a battery module was selected for analysis.

The conceptual design is based on the module design developed by the University of Waterloo team for the Battery Workforce Challenge (BWC), an Advanced Vehicle Technology Competition (AVTC) to design, build, and integrate a battery pack into a cargo van. In this work, the design serves as the basis for thermal analysis.

The module was intentionally designed to be simple and feasible for undergraduate students to lead, while also being structurally sturdy to serve as protective housing for the cells. The design considered easily sourced materials and simplified components to avoid dependence on specialized industrial equipment. Thermal considerations, module geometry, space constraints and material selection were analyzed with the aim of enabling effective heat transfer. Electrical components such as fuses, wiring, thermistors and busbars are excluded from the analysis, as the focus remains strictly on the thermal behavior of the cells. Overall, this chapter summarizes a simplified yet thermally functional module design, with the aim of establishing a foundation for thermal simulations intended to assess and enhance module cold-start performance.

4.2 Design considerations

4.2.1 Thermal management requirements

As part of the pack design, the thermal management system was planned at the pack level, with cold plates placed beneath several modules. Integrating cold plates that cover as much of the tray area as possible would simplify future pack assembly. Additionally, the risk of coolant leakage is significantly reduced by minimizing the number of inlets and outlets, which can only be achieved through pack-level

cooling. This design decision dictated the module's thermal requirements, which focused on enabling adequate heat dissipation from the cells and preventing the formation of hot spots through structural and material choices. The design layout prioritized open geometries to support air convection while maintaining the recommended cell to cell spacing provided by the manufacturer. It also aimed to maximize contact area with the pack's cold plates, ensuring an unobstructed thermal path and using contact materials with high thermal conductivity. In the same manner, the module shall promote unobstructed axial heat transfer to accommodate the heating strategies that will be introduced on top and discussed in the next chapter. Overall, these thermal requirements were intended to support the effective operation of the thermal management system.

4.2.2 Structural considerations and geometric constraints

The structural design of the module focused on mechanical integrity, thermal dissipation, cell alignment, and practicality. The module aimed to secure the cells firmly in place while maintaining open thermal pathways to support heat dissipation. The design focused on arranging the cells to fit as many as possible within the given width and length limitations. At the same time, the design included spacing between the cells enhancing mechanical strength and thermal performance which was previously highlighted by [39].

Regarding structural considerations, the module was designed for 21700 new cells operating under ideal conditions. Therefore, factors like cell swelling, gas generation, or changes in cell pressure due to cycling and aging [40] have not been considered. Expansion of cylindrical cells is generally not critical, and the low discharge rate of 0.3 C further supports the disregard of mechanical expansion and compression factors. However, this assumption is limited to low C rate values such as 0.3 C. This rate was established by the BWC managers for thermal simulations [41], likely due to safety considerations for a student-built system. Furthermore, the design relied on simplified estimations prioritizing a practical evaluation approach to exclusively support thermal simulations. Ultimately, the module design aimed to optimize the ratio of battery cells while ensuring both structural stability and supporting heat transfer as recommended by [40].

4.2.3 Material assessment criteria

The materials required for the proposed module were chosen based on a combination of functional and practical requirements tailored to a student-led development environment. The selected materials

needed to provide electrical insulation and support high thermal conductivity. At the same time, weight and manufacturability were important considerations. The module enclosure must protect the internal components while remaining lightweight, since most of the weight already comes from the cells, and a heavy battery pack can hinder the overall performance of the EV. Moreover, the materials shall comply with flame resistance (UL94 – 0) for safety reasons in the case of a thermal runaway event. Finally, the materials chosen were those that could be easily processed using equipment available at the university machine shop, ensuring that the design would be both feasible and realistic.

4.3 Design Description

The final design of the module is presented in Figure 10. It consists of seven main components, arranged from top to bottom.

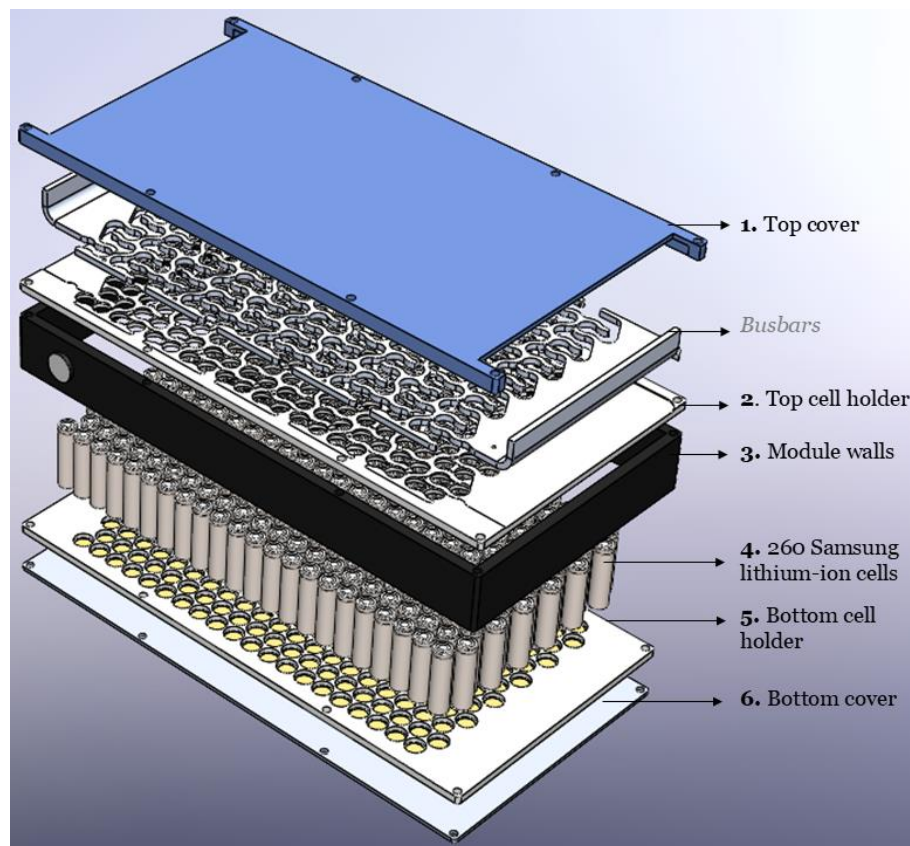


Figure 10. Battery module design

The top cover encloses the upper portion of the module. Beneath it, the busbars allow electrical connection between the cells. The top cell holder secures both the busbars and the upper ends of the

cells. The module walls provide lateral support along the sides. Within the walls, 260 Samsung lithium-ion cells are arranged in a hexagonal grid within the structure. Below the cells, the bottom cell holder supports their lower ends and includes thermal interface material (TIM) pads. Finally, the bottom cover seals the base of the module. These components will be described in detail below.

4.3.1 Top cover

The module top cover was designed to enclose the module and protect the busbar to cell connections from external environmental factors. A view of the top cover is presented in Figure 11.

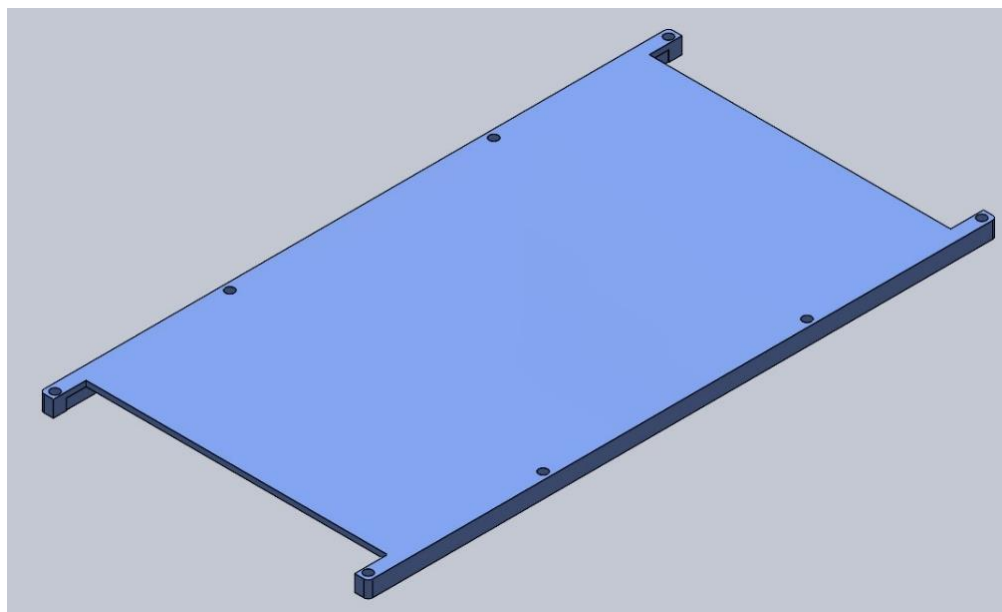


Figure 11. Isometric view of the battery module top cover

The top cover mainly serves as a protective element for the module internal components. Regarding material selection, the top cover was designed to be made of polycarbonate, selected for its high mechanical strength, low weight, and ease of procurement in sheet form. The lightweight nature of the polycarbonate was also a selling point aiming to avoid adding unnecessary weight to the module. The material is also suitable for CNC machining, making it suited for the proposed student design. The top cover includes cutouts that allow the busbar terminals to extend through, enabling future connections to other modules. Additionally, the open design around the terminals facilitates localized heat dissipation where thermal build up is expected. Through these conditions, the top cover design aims to provide mechanical protection and support the future integration of the module within the battery pack.

4.3.2 Top cell holder

The top cell holder was developed to secure the upper end of each cell, maintaining uniform spacing while ensuring electrical isolation. At the same time, this component holds the busbars firmly in place. The top cell holder design is presented in Figure 12.

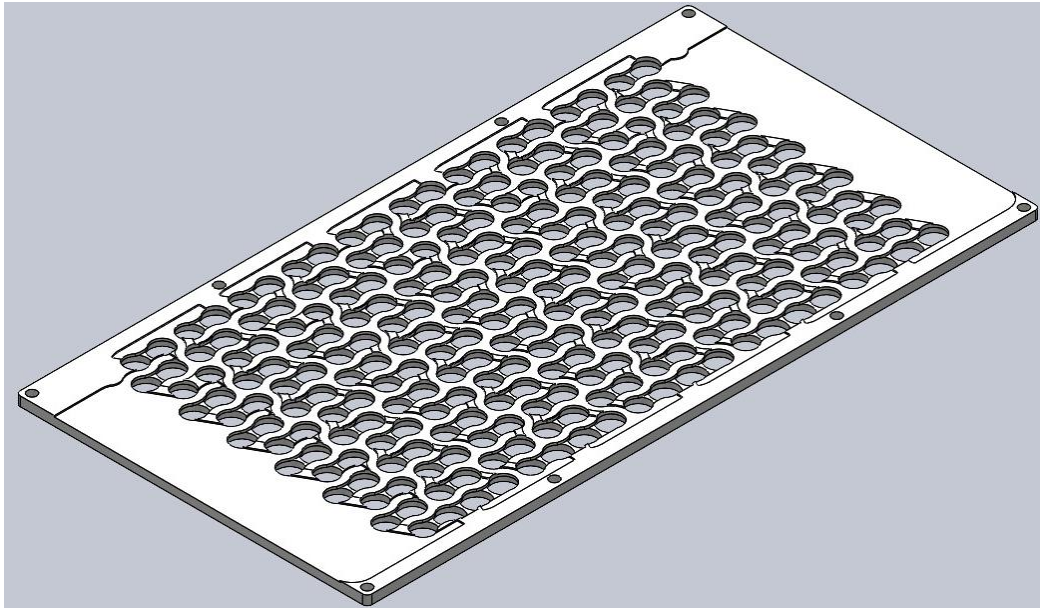


Figure 12. Isometric view of the battery module top cell holder

The top cell holder plays a structural role within the module. For material selection, polycarbonate was chosen. This material was selected for its mechanical strength, flame resistance, and dimensional stability. These properties are necessary to keep all components securely in place under mechanical and thermal stress. As previously mentioned, polycarbonate is compatible with CNC machining, which is essential given the complexity of the required features.

The design features cell-locating pockets on the underside of the top cell holder. These features hold each cell securely while ensuring the cells' top vents remain exposed and unobstructed, a safety requirement to allow for easy cell pressure relief if needed. On the other hand, raised sections on top of the top cell holder provide stable seating for the busbars, maintaining both electrical isolation and cell alignment across the module. From a thermal standpoint, the design encourages air circulation around the top of the cells, improving heat dissipation during operation. Overall, the top cell holder design balances mechanical support, electrical isolation and thermal considerations.

4.3.3 Module walls

The module walls were developed to seal the module and shield the cells from external environmental exposure. Figure 13 presents a view of the module walls.

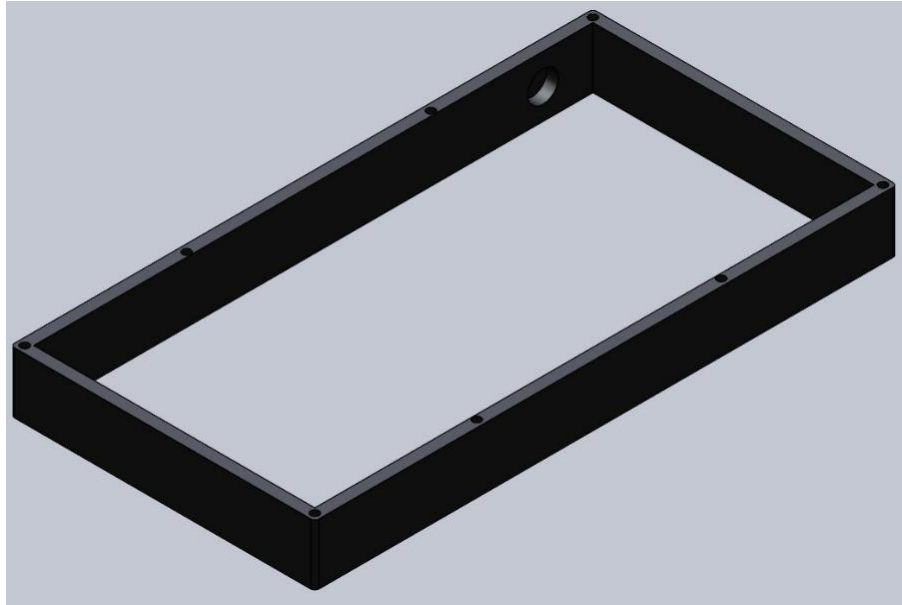


Figure 13. Isometric view of the battery module walls

As part of the structural design of the module walls, polycarbonate was also selected, consistent with previous module components, to provide electrical insulation between the cells and external users. This material choice is further supported by its use in battery testing enclosures, as highlighted by [42]. This example suggests that polycarbonate could be a solid choice to withstand the mechanical and thermal stresses present in thermal runaway scenarios.

The design features four walls arranged in a four-sided ring configuration, allowing for the insertion of eight fasteners to secure the entire module. Using polycarbonate enables straightforward manufacturing, either through 3D printing or by assembling prefabricated sheets. One trade-off of the design is limited heat dissipation because polycarbonate is not a good thermal conductor. As a result, heat is expected to dissipate more axially than radially, aligning with the top and bottom heat transfer areas. Despite this limitation, safety was prioritized, given polycarbonate's strong flame-retardant properties. Consequently, the module walls could help contain fire from spreading to nearby modules in a potential thermal runaway event. To sum up, the wall design prioritizes the safe containment and protection of the cell block.

4.3.4 Cells

The module was designed to house 260 Samsung 21700 lithium-ion cells, arranged vertically in a tightly packed configuration, as shown in Figure 14.

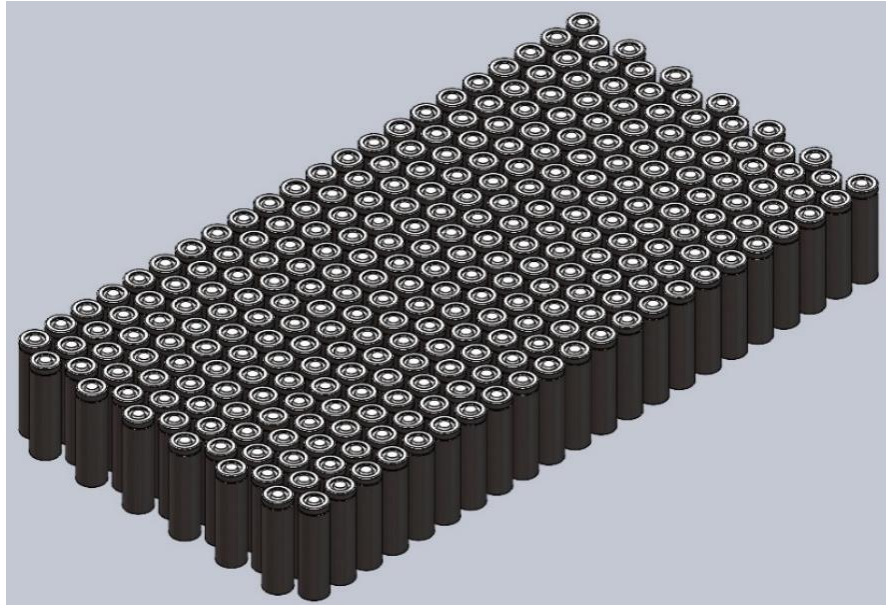


Figure 14. Isometric view of the battery module cell block

The cell arrangement design features a hexagonal configuration, chosen because it allows the cells to be packed more tightly, maximizing space efficiency within the module [2]. Additionally, based on the cell manufacturer's recommendations [43], a 2 mm gap between cells was maintained. This spacing ensures safety. As shown in [44], without any gap, adjacent cells exceeded the maximum temperature of a cell in a thermal runaway event. However, considering a 2 mm gap, their temperature was 3.5 times lower.

The vertical orientation of the cells supported the planned thermal management strategy. As found by [45], axial heat conduction is approximately four times greater than radial conduction in cylindrical cells, making the top and bottom surfaces the best pathways for heat transfer. Moreover, placing the cells with the vent facing up allowed that gas is released upward rather than toward neighboring cells in the event of thermal runaway, ensuring safety. Lastly, the uniform layout not only enhanced structural consistency but would also facilitate repeatable assembly across multiple modules. Overall, the cell arrangement balances compactness, thermal performance and safety constraints of the cells.

4.3.5 Bottom cell holder

Figure 15 presents the bottom cell holder used in the module design, which provides mechanical support while allowing thermal management. Integrated TIM pads in each slot improve heat transfer from the cells to the cooling structure below.

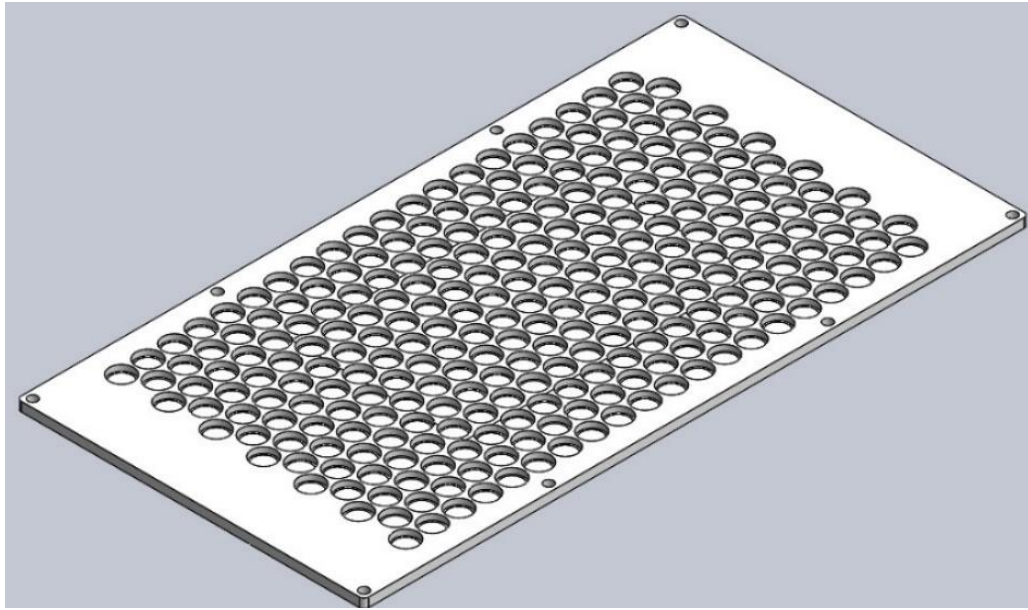


Figure 15. Isometric view of the battery module bottom cover

Polycarbonate was chosen as the material due to its high impact resistance, thermal stability, and ease of manufacturing. Using the same material for both the top and bottom holders ensures consistent thermal expansion and mechanical compatibility, reducing the likelihood of stress buildup or misalignment during operation. It also provides the necessary strength to support the cylindrical cells while keeping the overall design lightweight, which is important for EV applications.

The bottom cell holder design features a precise grid of circular openings that cradle each cell securely. These openings feature integrated locating elements that help position the cells accurately and prevent them from shifting during vibration. In addition, the layout of the holder supports ease of assembly.

Building on the material selection and mechanical design features of the bottom cell holder, thermal performance was a key aspect integrated into the overall module layout. Figure 16 illustrates the intended heat transfer path from the cell base to the cooling plate, emphasizing the role of the bottom cell holder containing the TIM pads in facilitating this flow.

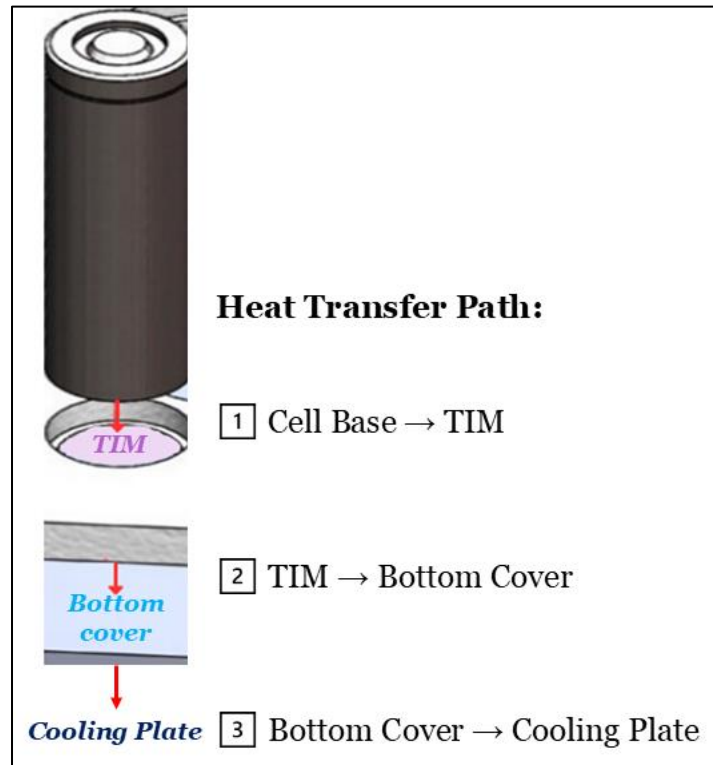


Figure 16. Heat transfer path from the cell base to the cooling plate through the TIM layer and bottom cover

Each slot of the bottom cell holder was designed to be filled with TIM pads with a thermal conductivity of 3 W/mK. These pads fill the gap between the cell surface and the bottom cover, allowing for improved heat transfer toward the cooling system underneath the module. This helps reduce thermal resistance at the contact surface and enables more uniform temperature distribution across the module. By combining structural support with enhanced thermal conductivity, the bottom holder contributes to the safety and performance of the overall battery design.

4.3.6 Bottom cover

The bottom cover, presented in Figure 17, was designed to enclose the underside of the module while also ensuring direct and uniform contact with the cold plate beneath it.

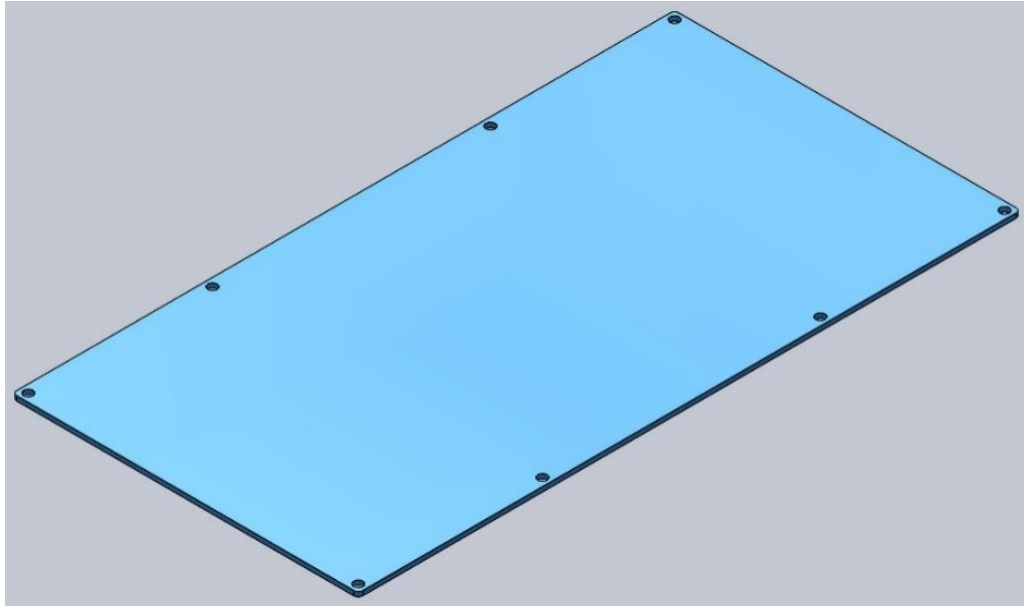


Figure 17. Isometric view of the battery module bottom cover

The bottom cover was designed to ensure effective heat transfer from the cells to the cold plate, while also serving as an interface that isolates all battery components from the external environment. Positioned directly beneath the bottom cell holder and TIM pads, its main function is to channel heat away from the base of the cells toward the cooling plate.

For the material selection, preference was given to non-conductive materials to enhance safety during assembly and future pack integration. Since the module sits on a metallic cold plate, the interaction between metal surfaces raised concerns about potential issues under vibration. While protective coatings on metallic interfaces were considered, they introduced additional complexity to manufacturing. Then, polycarbonate (PC) was initially evaluated due to its ease of use and lightweight properties, but its poor thermal conductivity (0.2 W/mK) [46] made it unsuitable for this application. As a consequence, CoolPoly [47], a thermally conductive polymer composite, was chosen. This material was selected due to its thermal conductivity (5.0 W/mK) and its UL 94 V-0 flammability rating [47], which ensures compliance with fire safety standards in high-voltage battery systems. It also combines moderate heat transfer capability with installation ease like PC, while maintaining a low weight that aligns with the module's design constraints.

In terms of design, the bottom cover features a flat, rectangular geometry. The flat profile ensures consistent surface contact with the cold plate, promoting efficient heat transfer from the battery cells. This minimalist design reflects its functional role as both a thermal interface and an environmental barrier.

4.4 Lessons Learned and Design Limitations

This module design presents a clean and practical layout for accommodating 260 Samsung cylindrical cells, but its thermal performance relies heavily on assumptions that introduce important limitations. Considering a cooling strategy at pack level, the module design assumes that the bottom surface is sufficient for transferring heat from the cells to the cold plate. This makes the thermal conductivity of the bottom cover and the contact resistance between the cell bases and the cover critical design parameters. Furthermore, the top and bottom cell holders offer electrical insulation and mechanical stability but introduce thermal resistance around the cell sides. Additionally, the top cover and busbar layer are thermally decoupled from the cold plate path, meaning heat must predominantly flow downward. Lastly, since there are no lateral or top-side cooling features, the design assumes that vertical heat conduction through the cell bottom is adequate under most operating conditions.

The analysis disregarded effects such as cell swelling, gas generation, or pressure changes due to aging were not considered, and these could compromise long-term structural and thermal integrity. Trade-offs were made to prioritize manufacturability, safety, and thermal accessibility.

Finally, while electrical components such as sensors, connectors, and busbars were not included in this analysis to keep the focus on cell-level thermal behavior, their role in measurement accuracy should not be overlooked. As shown in the previous chapter, lower experimental voltages may have been partially influenced by contact resistance effects during testing. Although these elements do not directly affect thermal distribution, they can compromise the reliability of voltage and temperature measurements if not properly accounted for. This highlights the importance of considering electrical interfaces in future designs, not for their thermal impact, but to ensure that measurements remain accurate and reflective of true cell behavior.

4.5 Summary of Findings

The conceptual module design supports thermal simulation by integrating key structural and material considerations that align with the expected heat flow behavior of cylindrical lithium-ion cells. The

design was developed to house 260 Samsung 21700 cells in a compact, electrically isolated configuration. From a thermal perspective, it leverages the fact that axial heat conduction is significantly more efficient than radial, guiding heat downward through the cell bases toward the cooling interface. To support this, the bottom of the module incorporates thermally conductive plastic paired with TIM pads to promote uniform heat transfer to the cold plate located at the pack level.

Polycarbonate was selected as the primary material for non-conductive components such as the top and bottom holders and enclosure walls. This choice reflects a balance between electrical insulation, fire resistance (UL 94 V-0), mechanical integrity, and weight reduction. Additionally, polycarbonate's compatibility with both CNC machining and 3D printing, particularly in sheet or film form, enabled the integration of precise cell locating features and a modular assembly strategy. While the design excludes active cooling or integrated sensing features, it was intentionally simplified to evaluate baseline thermal performance.

In summary, the module design integrates thermal functionality, material performance, and manufacturing feasibility to support controlled simulation studies, while leaving room for future enhancements such as switching to higher thermal conductivity materials for the base.

Chapter 5

Simulation and Analysis of Heating Strategies for the Battery Module

5.1 Introduction

The integration of heating elements within the battery module is examined through simulation, with a focus on evaluating how different power inputs perform under realistic boundary conditions and operating scenarios. By replicating cold-start environments, the analysis explores how heater configurations influence thermal response. The objective is to identify the configuration that improves cold-start performance while maintaining thermal safety and minimizing energy consumption.

5.2 Simulation model development

5.2.1 Simulation environment

The simulation model was developed based on the physical configuration of the student-designed cargo van battery module described in the previous chapter. This layout was adapted for use in the AVL CRUISE™ M simulation environment. The resulting setup, shown in Figure 18, retains the original 10s 26p electrical cell arrangement, available in Appendix C, and integrates Batemo 21700 cell data through an FMU package to accurately capture both electrothermal and thermal behavior.

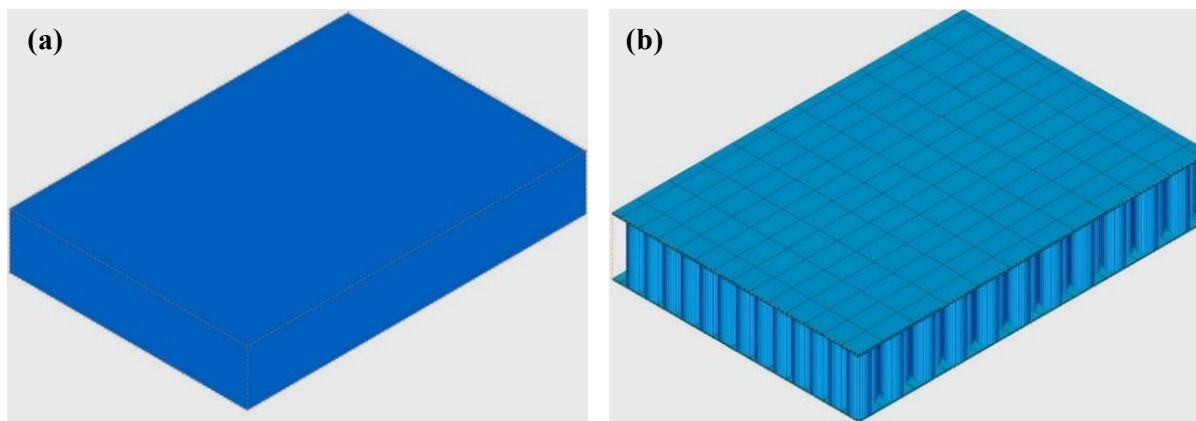


Figure 18. Battery module geometry used for simulation: (a) Simplified homogenized model used for thermal analysis, (b) Detailed configuration showing a simplified meshed structure and internal cell layout

5.2.2 Module Geometry and Simplification Strategy

To improve computational efficiency while maintaining thermal accuracy, the geometry was simplified by removing non-critical components such as fasteners, detailed busbar geometry, and cell spacers. The final model includes polycarbonate side walls, a polycarbonate bottom plate, and a two-layer top cover composed of polycarbonate and aluminum. Polycarbonate was represented in the simulations using the material properties of polypropylene, as this was the closest option available in the software database. These simplifications allow the simulation to focus on the dominant thermal interactions between the cells and surrounding structure. Two simulation configurations were developed to evaluate the thermal behavior of the battery module under cold-start conditions, with and without heating elements. Although both share the same physical layout, each is adapted to capture distinct thermal responses.

5.2.3 Simulation model without heating elements

Figure 23 introduces the first simulation configuration which represents the module operating without internal heating support. Its components and parameters are described in Figure 3.

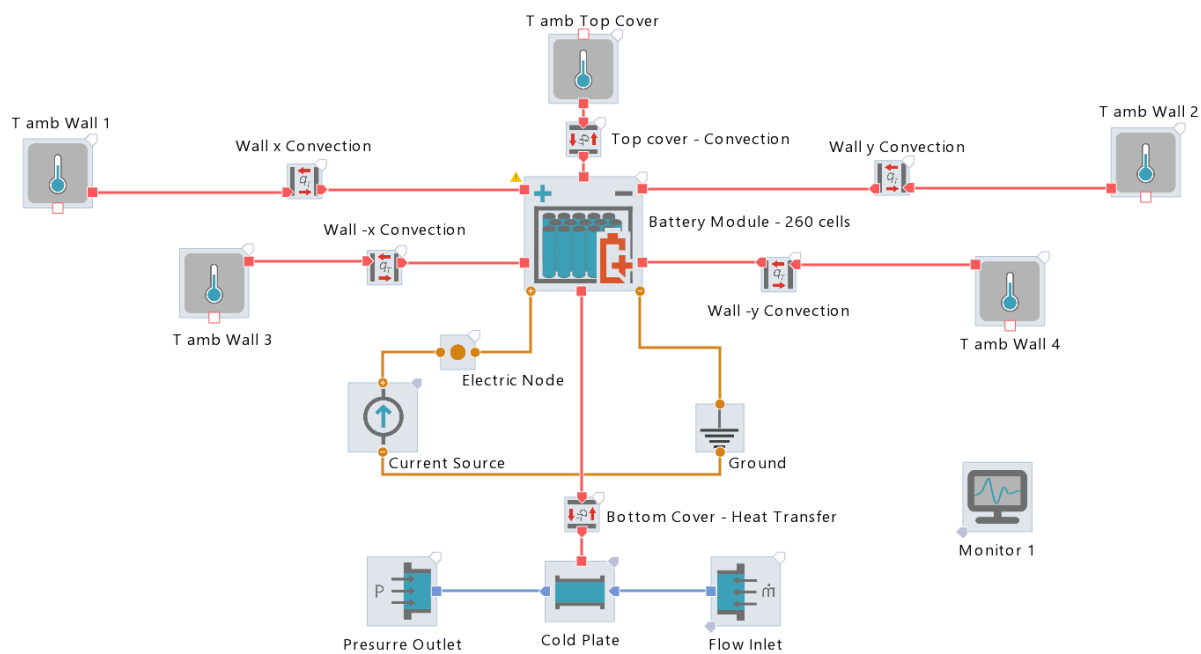


Figure 19. Simulation model configuration showing boundary conditions and component interactions for the unheated cold start scenario.

Table 7. Simulation components, descriptions and assigned parameter values for the unheated cold start scenario

Component	Description	Simulation <i>parameters</i> and values
Battery module – 260 cells	Thermal and electrical body under analysis	Previously described in section 5.2.2
Top Cover - Convection	Convection to ambient through the top surface	$A_z=173078 \text{ mm}^2$ $h = 20 \frac{W}{m^2K}$ [17]
<ul style="list-style-type: none"> • Wall x Convection • Wall -x Convection 	Convection boundaries on both lateral sides of the module	$A_x = 34530 \text{ mm}^2$ $h = 20 \frac{W}{m^2K}$
<ul style="list-style-type: none"> • Wall y Convection • Wall -y Convection 	Convection boundaries on front and back sides of the module	$A_y = 18030 \text{ mm}^2$ $h = 20 \frac{W}{m^2K}$
<ul style="list-style-type: none"> • T_{amb} Wall 1 • T_{amb} Wall 2 • T_{amb} Wall 3 • T_{amb} Wall 4 	Ambient conditions	$T_{amb} = -20 \text{ }^\circ\text{C}$
Electric Node	Distributes current input	NA
Current Source	Simulates discharge	$I = 127.4 \text{ A}$ per module (1C)
Ground	Electrical ground reference	NA
Bottom Cover – Heat Transfer	Heat transfer via cold plate	$A_z=54600 \text{ mm}^2$ $h = 20 \frac{W}{m^2K}$
Cold Plate	Cooling interface connected to the module bottom surface	Geometry = Rectangular Width = 590 mm Depth = 4 mm Length = 846 mm Propylene glycol/Water 50/50 [48] Friction coefficient = 0.06
Flow Inlet	Defines coolant flow into cold plate	$P_0 = 1 \text{ bar}$ $T_{amb} = -20 \text{ }^\circ\text{C}$ $\dot{m} = 0.267 \frac{kg}{s}$
Pressure Outlet		$P_f = 1 \text{ bar}$ $T_{amb} = -20 \text{ }^\circ\text{C}$
Monitor	Records data outputs	NA

5.2.4 Simulation model with external heating at the top cover

The second simulation configuration, presented in Figure 20, builds on the same physical layout and boundary condition framework presented previously, with one modification. In this case, the top cover is connected to an external heat source called Heating Element, enabling active heating during the cold start phase. All other components and boundary settings remain unchanged from the initial setup.

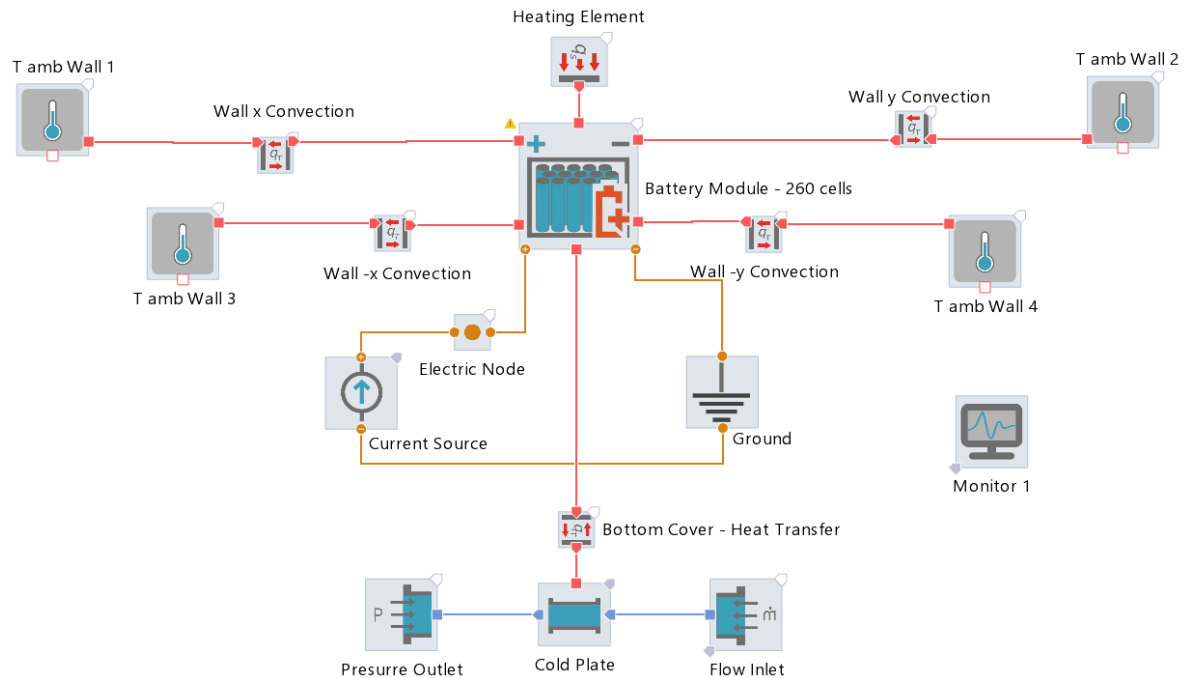


Figure 20. Simulation model configuration showing boundary conditions and component interactions for the heated cold start scenario.

To evaluate the feasibility of surface heating integration for cold-start enhancement, flexible heating strips manufactured by Bucan [49] were selected as a basis for the simulation setup. These strips are thin, rectangular, and flexible, making them suitable for integration onto flat or slightly curved surfaces [49]. In the model, the heating elements were defined as a continuous surface layer placed on top of the battery module, covering the same area as the top cover to ensure uniform heat distribution.

Bucan offers customizable heater designs that can target different geometries [49], making them well-suited for virtual prototyping. For this initial investigation, the lowest available power density (10 W/in²) was selected, resulting in a total constant heating power of 2683 W. This level was chosen to minimize energy consumption while still ensuring thermal support under cold ambient conditions.

5.2.5 Model assumptions and limitations

The simulation model is based on idealized conditions to isolate the impact of the heating strategy. All cells are assumed to be identical, balanced, and free from significant manufacturing or aging-related variations. A liquid-cooled cold plate is modeled at the bottom of the battery module. The inlet flow rate and temperature are defined as fixed inputs. The outlet is treated as a pressure outlet, assuming steady-state flow [48]. The model also assumes steady-state flow and outlet temperature profiles, as outlined in [30]. Additional assumptions adopted from [30] include steady-state and turbulent flow behavior, negligible thermal radiation effects, and constant thermophysical properties for both the battery materials and surrounding air. Uniform internal heat generation is assumed across all cells. Lastly, a constant current is drawn through the module using a current source. No variable load profiles or state-based electrical control logic is applied.

5.3 Methodology for evaluating heating integration strategies

To evaluate the feasibility of integrating heating elements to enhance performance during cold start conditions, three key factors were evaluated at multiple levels. The first factor is the heating strategy, which includes four cases as detailed in Table 8. Each case varies in terms of heating configuration, power source, and whether the battery is actively discharging.

Table 8. Description of the four simulated heating scenarios applied to the battery module.

Case	Heating Strategy	Heating Power Source	Battery operation (1C discharge)	Description
A	No heating element	–	On	Baseline configuration. No heating is applied. The battery operates.
B	Surface heating element	External	On	Heating elements are externally powered. The battery operates.
C	Surface heating element	External	Off	Heating elements are externally powered. The battery does not operate.
D	Surface heating element	Internal (from battery)	On	This is a hypothetical case. The battery operates to power the heating elements.

Figure 21 provides a visual overview of the four simulated heating strategies. Each case shows a different combination of heating element integration, heater power source and battery operation.

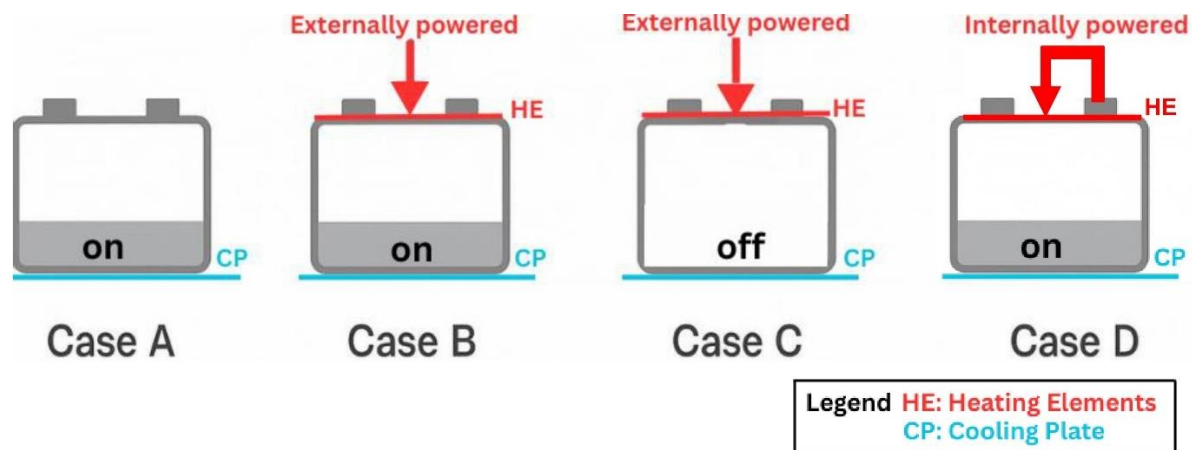


Figure 21. Visual representation of the four simulated heating configurations. HE: Heating Elements; CP: Cooling Plate. "On" indicates battery operation; "Off" indicates no discharge.

The second factor is the ambient temperature, with three below zero temperatures considered: $-20\text{ }^{\circ}\text{C}$, $-10\text{ }^{\circ}\text{C}$ and $0\text{ }^{\circ}\text{C}$. These levels were selected to reflect typical winter startup conditions in cold climates considering the operating range restricted by the cell manufacturer [34]. The third factor is the initial SOC, evaluated at 80%, 50% and 20%. These levels capture the typical upper and lower bounds of recommended battery usage, including a mid-range value for comparison. To assess the impact of these factors on cold start performance, two key outcomes were monitored: the time required for the module to reach $10\text{ }^{\circ}\text{C}$ and the final SOC after the heating or discharge process.

5.4 Results - Cold discharge with and without external heating

To isolate the influence of ambient temperature, only Case A and Case B were considered in this initial comparison. These cases represent two extremes: the absence of thermal support versus the external-thermally assisted scenario.

5.4.1 Temperature rise profile at different ambient temperatures

The plots presented below in Figure 22 show the evolution of module temperature over time at different ambient temperatures, highlighting the extent to which external heating improves thermal performance during cold discharge.

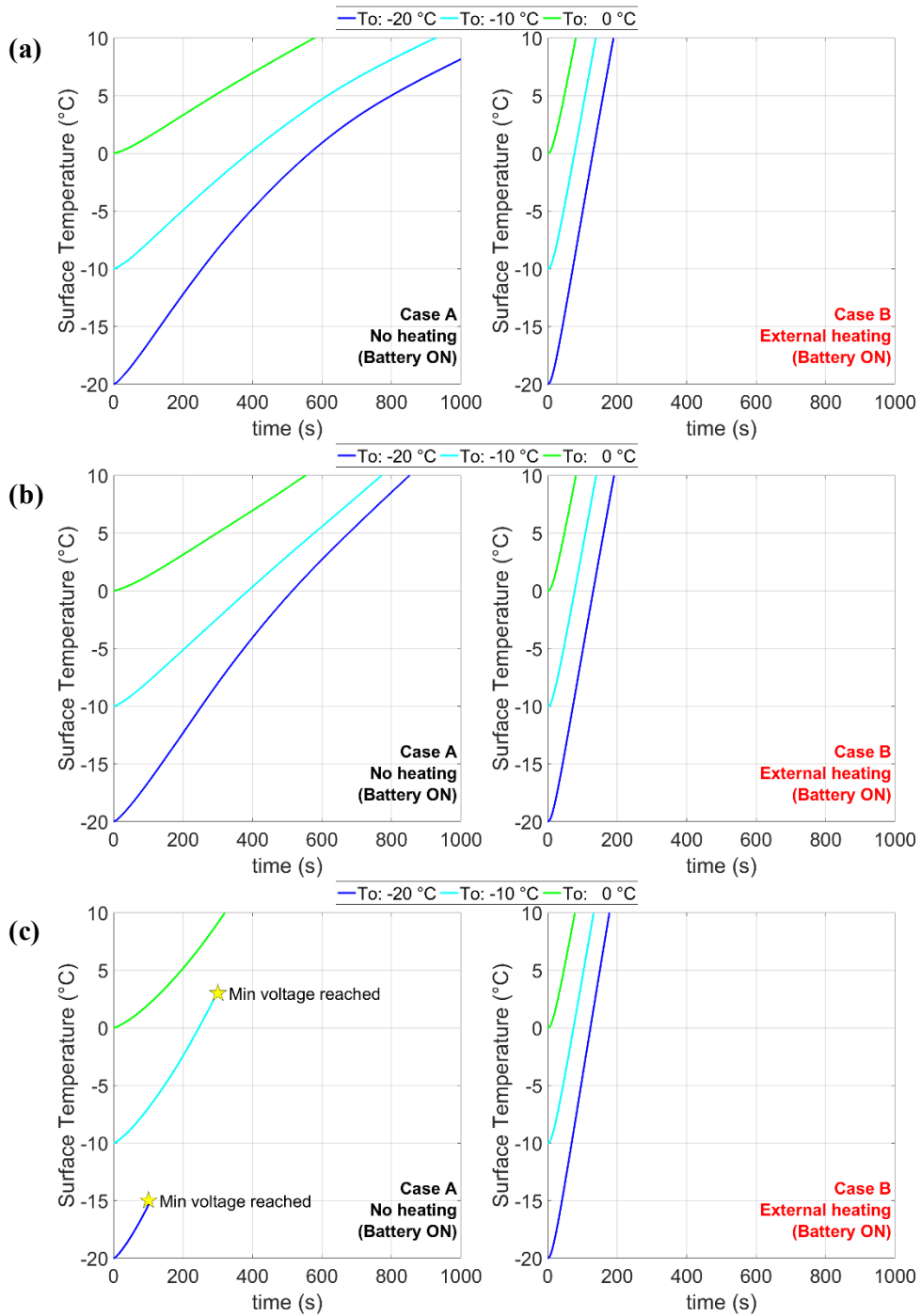


Figure 22. Surface temperature evolution of a 21700 lithium-ion cell for Case A: no heating and Case B: external heating, under cold-start conditions at initial SOC levels of (a) 80%, (b) 50%, and (c) 20%, and ambient temperatures of -20 °C, -10 °C, and 0 °C.

At all three initial SOC levels (80%, 50%, and 20%), and across the three ambient temperatures (-20 °C, -10 °C, and 0 °C), the application of external heating (Case B) consistently results in significantly faster temperature increases compared to the cold operation without the heating elements (Case A). The temperature profiles under Case B are steep and reach 10 °C well before 400 s in most cases, regardless of the initial SOC or ambient temperature. In contrast, the temperature curves for Case A show a much slower warming rate, with surface temperatures often remaining below 0 °C even after 800 seconds.

The benefit of heating elements is most prominent at the lowest ambient temperature (-20 °C). In this condition, Case A exhibits the slowest thermal response, with battery temperatures staying below freezing temperatures for extended durations. However, under Case B, the module rapidly surpasses 0 °C and approaches the target temperature, demonstrating the heater's ability to overcome below zero initial thermal temperatures.

The effectiveness of external heating is also robust across different initial SOC levels. Even at 20% SOC, the lowest tested, the heating system in Case B ensures the battery reaches optimal operating temperatures quickly. On the other hand, in Case A, low SOC leads to limited internal heat generation, making it insufficient to warm the cell. Notably, in the 20% SOC and -20 °C scenario under Case A, a low voltage cutoff is reached (as marked by the yellow star) before the surface temperature could rise meaningfully, emphasizing that without heating, low SOC operation at low temperatures is unfeasible.

The superior thermal performance observed with external heating can be attributed to the direct and sustained energy input provided by the heaters, which is independent of the battery's internal state. At low ambient temperatures and low initial SOC, the battery generates minimal internal heat due to reduced electrochemical activity and limited current availability. This makes self-heating slow and unreliable. In contrast, heaters supply a consistent thermal flux that raises the surface temperature rapidly, by passing the limitations of electrochemical heat generation. Lastly, the heater's power delivery is not constrained by the battery's voltage or current limits.

To further quantify the impact of external heating under cold start conditions, Table 9 presents the time required for the module surface to reach 10 °C across various initial SOC levels and ambient temperatures, comparing Case A and Case B under cold operation.

Table 9. Comparison of module heating time to reach 10 °C with and without external heating at different ambient temperatures (-20 °C, -10 °C, 0 °C) for 80%, 50% and 20% initial SOC

Initial SOC (%)	Ambient temperature (°C)	Time to reach 10 °C (s)		Time reduction (A → B) %
		Case A	Case B	
80	-20	1128	190	83
	-10	929	139	85
	0	579	81	86
50	-20	853	192	77
	-10	773	140	82
	0	554	82	85
20	-20	101 (-15 °C)*	178	NA
	-10	293 (2 °C)*	133	NA
	0	321	79	75

*Module min voltage (25 V) reached

The data reveals the benefit from using external heating to reduce the time required for the module to reach 10 °C. Across all combinations of ambient temperature and initial SOC, heating elements lead to substantial reductions in warm-up time, ranging from 75% to 86% when compared to no heating cold operation (Case A). The time savings are most pronounced at milder ambient temperatures (0 °C), where heating is more efficient due to the smaller thermal gap to overcome. At 80% and 50% SOC, time reductions are consistently high (77 to 86%) regardless of ambient temperature, demonstrating that external heating is effective even when the cell’s own internal heat generation varies. Lastly, at 20% SOC the values for Case A at -20 °C and -10 °C are marked with an asterisk, indicating that the module could not safely complete the operation due to early voltage cut-off. Notably, in these same scenarios, external heating still enables the module to reach 10 °C in under 178 seconds, emphasizing its essential role in ensuring operability under cold conditions.

The resulting temperature distributions (at 3 different times) for Cases A and B considering the same conditions (50% and -20 °C) are shown in Figure 23. These visualizations provide a general overview of how the surface temperature evolves during the heating process and support the trends discussed in the previous section.

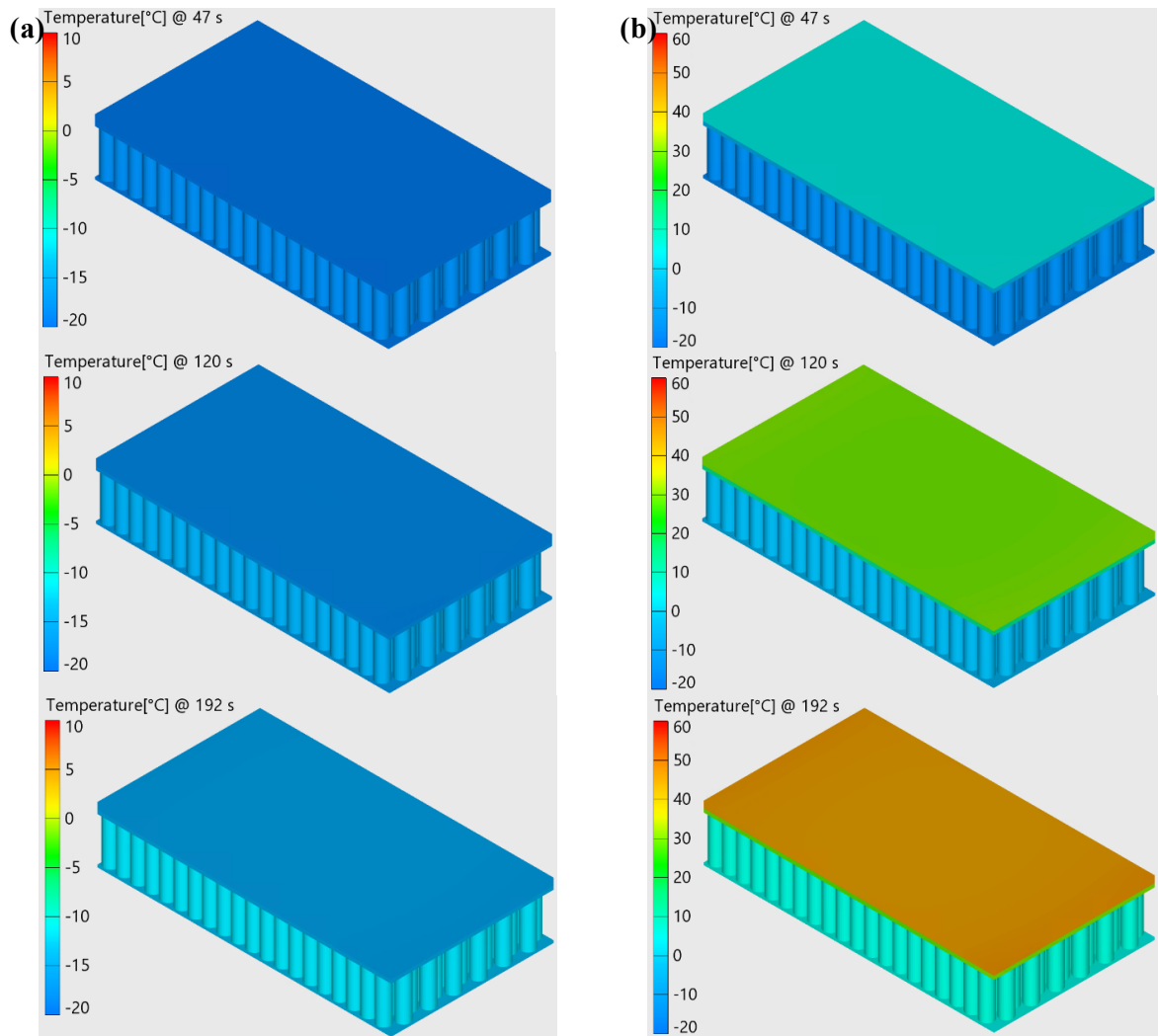


Figure 23. Evolution of temperature distributions over time at -20 °C and 50% initial SOC for (a) Case A and (b) Case B. The walls are hidden to visualize the effect on the 21700 cells block.

At 50% initial SOC, the simulation results show the module's thermal behavior under two conditions. In Case A (Figure 29a), where no external heating is applied, the cells heat themselves through internal losses, but the temperature remains below zero. In Case B (Figure 29b), with surface heating, the top surface reaches the highest temperature and the cells themselves reach 10 °C within 192 s, highlighting the effectiveness of the heating strategy. However, it is important to note that these results are based on a simplified representation, and the temperature distributions reflect overall trends rather than precise spatial variations. The observed surface temperature gradients suggest that localized heating effects

may occur, but the cell temperatures and full thermal uniformity cannot be fully resolved with this model.

To better understand the detailed temperature distribution, heat transfer pathways, and potential hotspots within the module, further analysis using 3D simulations is recommended. These would provide a more accurate depiction of spatial thermal behavior and help validate the assumptions made in this study. For now, the presented results serve as a general estimation of the heating effect.

5.4.2 Final SOC's at different ambient temperatures

Beyond warm-up time, the final SOC was evaluated across different initial SOC levels to assess energy retention during cold discharge. Table 10 presents the decrease in SOC during cold-start operation, comparing Case A and Case B across different initial SOC levels and ambient temperatures.

Table 10. Comparison of SOC decrease during cold operation with and without heating for initial SOC of 20%, 50%, and 80% at different ambient temperatures (-20 °C, -10 °C, and 0 °C)

Ambient temperature (°C)	Initial SOC (%)	Case A		Case B	
		Final SOC (%)	SOC decrease (%)	Final SOC (%)	SOC decrease (%)
-20	80	48	34	74	6
	50	26	24	44	6
	20	0*	20*	15	5
-10	80	54	26	76	4
	50	28	22	46	4
	20	0*	20*	16	4
0	80	63	17	77	3
	50	34	16	47	3
	20	11	9	17	3

*Module min volage (25 V) reached

Table 10 demonstrates how the initial SOC influences the discharge performance of the battery module during cold operation. In Case A, which lacks external heating, the battery consistently experiences greater SOC reduction and, in some cases, fails to complete the discharge highlighting the vulnerability of low-SOC operation under cold conditions. In contrast, Case B, with externally powered heating,

shows a significantly smaller SOC decrease across all conditions, even at 20% initial SOC. In these scenarios, the battery avoids premature voltage cut-off and retains 15–17% final SOC, indicating a more stable and complete discharge. This improvement suggests that heating helps preserve usable charge by maintaining internal conditions that prevent rapid voltage drop, which is especially critical when operating near the lower SOC limit.

An interesting observation in Case B is that the SOC decrease remains nearly constant across all initial SOC levels for a given temperature. For instance, at -20 °C, the SOC decrease is consistently around 5 to 6% whether the battery starts at 80%, 50%, or 20% SOC. This suggests that the heating system provides sufficient thermal support to stabilize the battery's internal resistance and voltage response, regardless of how much charge is initially available. As a result, the battery can discharge proportionally to its starting SOC without being limited by cold-induced inefficiencies. This behavior reflects a uniform improvement in electrochemical accessibility enabled by heating, making the discharge process more linear and predictable.

Furthermore, at lower initial SOC levels, the battery exhibits higher internal resistance, leading to a faster rate of heat generation and a quicker rise in temperature. As a result, low SOC cases reach the 10 °C threshold faster than high SOC cases. In contrast, higher initial SOC levels result in slower temperature rise. This highlights a trade-off where low SOC enables faster initial warming, while high SOC might support more extended heating.

Overall, the results confirm that low initial SOC significantly limits discharge capability during cold starts, primarily due to early voltage cut-off. External heating mitigates this limitation by enabling better access to the remaining charge, making it particularly valuable when operation must begin at reduced SOC levels.

5.5 Results - Heating behavior with and without battery discharge

This section compares Cases B and C to evaluate how battery discharge influences the heating behavior when external surface heating is applied. Both cases use external heating, but only Case B includes battery discharge. This comparison isolates the thermal contribution of the battery under load versus idle conditions. The time taken for the battery module to reach 10 °C under each condition is shown in Table 11.

Table 11. Comparison of module heating time to reach 10 °C with external preheating (no operation) and external heating during cold operation at ambient temperatures of -20 °C, -10 °C, and 0 °C

Ambient temperature (°C)	Time to reach 10 °C (s)		Time reduction (C → B) %
	Case C	Case B	
-20	226	178	21
-10	157	133	15
0	88	79	10

The 20% initial SOC condition was selected for Case B, as this level exhibits the highest internal resistance among the tested SOC values. However, as Case C involves no battery operation and is simulated using a 0 A current, any variation in internal resistance or heating due to SOC level is not present in the non-operating scenario. As a result, this comparison produces the greatest internal heat during discharge, highlighting the maximum possible impact of using the battery as an additional thermal source under external heating.

The comparison between Cases B and C shows the effect of internal heat generation from battery discharge. Across all ambient temperatures, Case B consistently shows faster heating, confirming that battery discharge contributes additional thermal energy that enhances the overall heating rate. This difference is most significant at -20 °C, where the battery’s internal resistance is highest, resulting in greater Joule heating as current flows. At this temperature, the heating time is reduced by 21%, which is a substantial improvement when rapid warm-up is critical for performance. As the ambient temperature rises, the gap narrows, indicating that the relative contribution of internal heat decreases under milder conditions.

Although the absolute reduction in heating time ranges from 9 to nearly 48 seconds, depending on the case, these values represent meaningful improvements in real-world applications where every second counts such as preventing system delays during startup. Therefore, even though external heating is the primary driver, battery discharge offers a valuable contribution, especially in the most challenging thermal conditions.

5.6 Results - Battery-Powered Heating Feasibility

This section evaluates the hypothetical case (Case D) whether the battery could realistically power its own heating elements system during cold-start conditions. The assessment is based on energy availability and thermal requirements, drawing from the results of Cases A and B. Case A provides information on how much energy the battery can deliver under cold discharge without any external heating as shown in equation (9).

$$\mathbf{Usable\ energy}_{battery} = \mathbf{Energy}_{battery\ (SOC_0 \rightarrow 0\%)} \quad (9)$$

In contrast, Case B captures the total energy required by the external heating system to bring the module to the target temperature with battery discharge represented. The energy is calculated using the constant power applied to the heating elements over the previously determined heating duration t_B . The energy required by the heating elements is presented in equation (10).

$$\mathbf{Energy}_{heater} = \mathbf{Power}_{heater} \times t_B \quad (10)$$

By comparing the energy delivered in Case A to the energy consumed by the heater in Case B, it is possible to determine if the battery holds sufficient capacity to self-power its heating element, and under what initial SOC and temperature conditions this would be viable. The heating energy ratio was calculated to evaluate the proportion of battery energy required to power the heating system. It is defined in equation (11)

$$\mathbf{Heating\ energy\ ratio} = \frac{\mathbf{Energy}_{heater}}{\mathbf{Energy}_{battery\ (SOC_0 \rightarrow 0\%)}} \times 100 \quad (11)$$

5.6.1 Effect/Feasibility of self – heating

Table 12 shows the results of the energy comparison between the heating demand and the usable battery energy across different ambient temperatures and initial SOC levels. These values form the basis for evaluating the viability of battery-powered heating under cold-start conditions.

Table 12. Comparison of required energy to power the heating elements and usable battery energy at different ambient temperatures and initial SOC levels

Initial SOC (%)	Ambient Temperature (°C)	Required energy heater (kJ)	Usable energy battery (kJ)	Heating energy ratio (%)
80	-20	509.8	11529.5	4
	-10	372.9	11804.8	3
	0	217.3	12016.9	2
50	-20	515.1	6196.59	8
	-10	375.6	6520.59	5
	0	220.0	6862.73	3
20	-20	477.6	346.43	100*
	-10	356.8	1025.71	35
	0	212.0	1497.09	14

**Energy_{battery} < Energy_{heater}*

The results highlight how the feasibility of battery-powered heating depends strongly on both ambient temperature and initial SOC. At higher initial SOC levels (80% and 50%), the battery consistently provides far more usable energy than is required by the heating system. For example, at -20 °C and 80% initial SOC, the heating energy demand is 509.8 kJ, while the battery can supply over 11529.50 kJ meaning just 4% of the available energy will be used for powering the heating elements. Even at -20 °C and 50% initial SOC, the battery still retains a comfortable energy margin, with heating representing only 8% of its usable capacity. This indicates that at medium to high SOC levels, battery-powered heating is entirely feasible with minimal impact on overall energy availability.

However, at 20% SOC, the energy margin becomes far more constrained, especially under severe cold. At -20 °C, the battery can only deliver 346.43 kJ, which is less than the required 477.6 kJ for heating, making self-powered heating infeasible. At -10 °C and 0 °C, the battery fares are better at 20% initial SOC, but the heating energy still accounts for a large share of usable energy: 35% and 14% respectively. These high ratios suggest that while self-powered heating may be possible at 20% initial SOC in milder conditions, it would leave little remaining energy for vehicle propulsion or other systems.

Overall, the findings indicate that self-powered heating is viable at moderate to high SOC levels across all tested temperatures, but its feasibility becomes limited at low SOC, especially under severe cold,

due to restricted energy availability. This highlights the importance of employing external powered heating strategies when expecting cold-start operation at low charge levels.

5.7 Design implications and future work

The analysis highlights key design limitations for battery-powered heating under cold-start conditions. Significant energy is required not only to raise the module temperature but also to overcome heat losses to the environment, limiting the energy available for functional operation. Lastly, the fixed heater power approach lacks adaptability, and the lumped model overlooks internal temperature gradients. Future work should explore dynamic heating control, improved insulation, integration with load operation, and more detailed thermal modeling to enable safer and more energy-efficient cold-start strategies.

5.8 Summary of findings

The simulation results highlight the significant influence of heating strategy, ambient temperature, and initial SOC on cold-start performance. Among all factors, the presence of active operation and external heating had the greatest effect in reducing the time required to reach 10 °C, particularly under extreme cold conditions (-20 °C). Configurations without heating (Case A) struggled to reach the target temperature within acceptable timeframes, requiring over 1000 s at -20 °C and 80% SOC, and were entirely unable to warm up the battery at 20% SOC before hitting the module's minimum voltage limit.

Case B, which applies external heating during discharge, consistently demonstrated the most effective thermal response. It reduced the time to reach 10 °C by 77 to 86% compared to the baseline (Case A), requiring as little as 79 to 192 s across all SOC levels and ambient conditions. SOC loss during cold operation was significantly higher in Case A, reaching 34% at -20 °C and 80% SOC, compared to only 6% in Case B under the same conditions. Compared to external preheating without discharge (Case C), Case B also showed improvements, achieving 10 to 21% faster heating times depending on ambient temperature. Notably, only external preheating (Case C) reached 10 °C in 226 s at -20 °C, while Case B achieved the same in 178 s, highlighting its advantage for simultaneous warm-up and operation.

Using battery discharge to heater (Case D) resulted in a high heating energy demand. At 20% SOC and -20 °C, the usable energy (346.43 kJ) was insufficient to power the heater (477.6 kJ), rendering self-heating unviable. Even at higher SOC levels, internal heating consumed 8% and 4% of available battery energy at 50% and 80% SOC, respectively. These values illustrate a clear trade-off between warm-up performance and usable energy, especially under extreme cold.

Overall, the findings support the integration of external heating strategies, particularly external heating during operation (Case B) or external preheating (Case C), to ensure reliable cold-start performance. These strategies enable rapid temperature recovery while preserving battery energy for driving. Their effectiveness is especially pronounced under low SOC and extreme cold, where internal heating becomes functionally infeasible.

Chapter 6

Conclusions and Recommendations

6.1 Key Findings

This study explored the cold-start behavior of 21700 cylindrical lithium-ion cells and modules using thermal system simulation, supported by experimental validation and conceptual design work. The research was structured into three interconnected components: cell-level thermal characterization, module design for thermal transfer, and the evaluation of integrated surface heating strategies. Together, these chapters formed a comprehensive investigation into the feasibility and effectiveness of various thermal approaches under cold ambient conditions, contributing new insight into how structural design, material selection, and heating methods interact in shaping battery cold-start performance.

At the cell level, both experimental testing and simulation revealed the significant impact of ambient temperature on the cell performance. Discharge capacity and voltage dropped substantially under cold conditions, particularly at $-12\text{ }^{\circ}\text{C}$ and low SOC levels. While convective boundary simulations followed the same trend as the experimental results, the latter showed a lower voltage response due to additional resistance in the setup. In contrast, adiabatic models overpredicted performance. The analysis confirmed that lithium-ion cells alone cannot self-heat adequately under severe cold-start conditions, as real-world temperature rises were minimal. This chapter highlights the limitations of relying solely on internal heat generation and emphasizes the importance of incorporating thermal support in low-temperature environments.

Building on this, a conceptual module was designed to explore structural and material strategies that support thermal management. The design prioritized axial heat transfer through the base of each cell to a cold plate, using thermally conductive plastic and TIM pads to improve interface quality. Polycarbonate was selected for the rest of the components due to its manufacturability, electrical insulation, and flame resistance, but its low thermal conductivity limits passive heat dissipation. While the design excluded embedded sensors, it created a modular foundation for thermal evaluation and demonstrated how material selection and cell alignment can be tailored to facilitate thermal simulation. This chapter reflected the trade-offs between manufacturability, safety, and thermal performance, identifying clear pathways for future module enhancements, such as incorporating higher-conductivity base materials.

To improve thermal performance, the final stage of this thesis integrated surface heating elements and simulated their impact under various initial SOC and ambient temperature scenarios. The findings showed that external heating during discharge dramatically reduced warm-up times, by up to 86%, and prevented premature voltage cut-offs at low SOC and $-20\text{ }^{\circ}\text{C}$. External preheating alone offered energy-efficient thermal recovery. In contrast, internal battery-powered heating was only viable above 50% SOC. At extreme cold and 20% SOC, internal heating became infeasible due to the heater's energy demand exceeding the battery's available energy. This chapter confirmed that external heating strategies are not only more effective but also critical for maintaining operational readiness in sub-zero conditions. Moreover, heating strategies contributed to significantly lower SOC loss during discharge, reinforcing their value in preserving usable energy.

Collectively, this research contributes new knowledge to the field of battery thermal management by integrating material-aware module design with dynamic heating simulations. It demonstrates the importance of aligning structural design with realistic boundary conditions and quantifies the energy trade-offs of different heating approaches. The study also showcases how a simulation-led approach, grounded in experimental data and practical design considerations, can guide early-stage thermal strategy development. Lastly, this work highlights the need for integrated, application-specific thermal solutions and lays the foundation for future optimization of heating control, module architecture, and real-time thermal diagnostics.

6.2 Limitations

The use of thermal system simulation offered a computationally efficient means to evaluate axial heat flow but inherently excluded localized heating effects, which may arise in real operating conditions. Experimental validation was performed at cell level and is yet to be seen at module level. The thermal boundary conditions used in simulation were idealized, assuming uniform contact resistance and perfect interface bonding between components. In practice, inconsistencies in compression, flatness, or extra materials such as adhesives could affect heat transfer efficiency. Moreover, the thermal influence of electrical components such as busbars, connectors, and BMS circuitry was not included, although they may restrict heat dissipation paths.

The module-level simulations, while conceptually aligned with the physical design, did not account for 3D mechanical effects that could affect long-term thermal reliability. Additionally, heating scenarios involving externally powered elements assumed continuous access to power infrastructure, which may

not always be feasible in real-world settings. Finally, the study focused on static heating profiles without integrating real time thermal control or safety mechanisms. Thermal runaway behavior was outside the scope of this work but represent important areas for future investigation. Together, these limitations define the boundaries of the current study and point toward opportunities for more advanced modeling and experimental validation in future research.

6.3 Recommendations for Future Work

To build on the findings of this study, several areas are recommended for further investigation. The implementation of on/off control logic for the heating elements should be explored. The current study applied constant heating power, but a time dependent or feedback-based control strategy could improve energy efficiency by activating the heater only, when necessary, based on cell temperature or SOC thresholds. Furthermore, there is a need to optimize the location and coverage of the heating elements across the module. Strategic placement could reduce hotspots, improve thermal uniformity, and minimize energy use. Alongside this, the surface temperature of the heating elements should be carefully understood to avoid thermal overshoot and ensure user safety. Finally, moving beyond thermal system simulation, 3D simulations should be conducted to capture spatial thermal gradients, edge effects, and detailed geometry-dependent interactions. A 3D approach would also allow for more realistic modeling of the module structure, including airflow paths, cell-to-cell variations, and thermal asymmetries, providing a more robust foundation for design validation and system-level integration.

References

- [1] K. S. Garud, L. D. Tai, S.-G. Hwang, N.-H. Nguyen, and M.-Y. Lee, “A Review of Advanced Cooling Strategies for Battery Thermal Management Systems in Electric Vehicles,” *Symmetry*, vol. 15, p. 1322, June 2023, doi: 10.3390/sym15071322.
- [2] I. Torrano, J. Martín-Ortiz, J.-L. Dauvergne, Á. Serrano, and D. Bielsa, “Thermal optimization of cylindrical lithium-ion hybrid thermal management system based on shape-stabilized phase change materials under realistic operating conditions,” *Journal of Power Sources*, vol. 617, p. 235148, Oct. 2024, doi: 10.1016/j.jpowsour.2024.235148.
- [3] Transport Canada, “Canada’s Zero-Emission vehicle sales targets,” AHSB 17484854. Accessed: July 13, 2025. [Online]. Available: <https://tc.canada.ca/en/road-transportation/innovative-technologies/zero-emission-vehicles/canada-s-zero-emission-vehicle-sales-targets>
- [4] J. Zhang *et al.*, “Experimental study on the low-temperature preheating performance of positive-temperature-coefficient heating film in the prismatic power battery module,” *Applied Thermal Engineering*, vol. 258, p. 124798, Jan. 2025, doi: 10.1016/j.applthermaleng.2024.124798.
- [5] M. Waseem, T. R. Rao, and K. S. Reddy, “Challenges, advances, and perspectives of battery thermal management cooling techniques in EVs,” *Future Batteries*, vol. 7, p. 100096, Sept. 2025, doi: 10.1016/j.fub.2025.100096.
- [6] S. R. Shinde, Y. Song, and E. Sahraei, “Modeling Electric Vehicle’s Battery Module using Computational Homogenization Approach,” *International Journal of Energy Research*, vol. 2023, no. 1, p. 9210078, 2023, doi: 10.1155/2023/9210078.
- [7] Y. Wu, Ed., *Lithium-Ion Batteries: Fundamentals and Applications*. Boca Raton: CRC Press, 2015. doi: 10.1201/b18427.
- [8] C. Lin *et al.*, “Heat generation quantification of high-specific-energy 21700 battery cell using average and variable specific heat capacities,” *Applied Thermal Engineering*, vol. 184, p. 116215, Feb. 2021, doi: 10.1016/j.applthermaleng.2020.116215.
- [9] T.-F. Yang, P.-Y. Lin, L.-T. Teng, S. Rashidi, and W.-M. Yan, “Numerical and experimental study on thermal management of NCM-21700 Li-ion battery,” *Journal of Power Sources*, vol. 548, p. 232068, Nov. 2022, doi: 10.1016/j.jpowsour.2022.232068.

- [10] Y. Kato, Z. Ogumi, and J. M. P. Martín, Eds., *Lithium-Ion Batteries: Overview, Simulation, and Diagnostics*. New York: Jenny Stanford Publishing, 2019. doi: 10.1201/9780429259340.
- [11] P. R. Tete, M. M. Gupta, and S. S. Joshi, “Developments in battery thermal management systems for electric vehicles: A technical review,” *Journal of Energy Storage*, vol. 35, p. 102255, Mar. 2021, doi: 10.1016/j.est.2021.102255.
- [12] Y. Wang, X. Zhang, and Z. Chen, “Low temperature preheating techniques for Lithium-ion batteries: Recent advances and future challenges,” *Applied Energy*, vol. 313, p. 118832, May 2022, doi: 10.1016/j.apenergy.2022.118832.
- [13] C. Bibin, M. Vijayaram, V. Suriya, R. Sai Ganesh, and S. Soundarraaj, “A review on thermal issues in Li-ion battery and recent advancements in battery thermal management system,” *Materials Today: Proceedings*, vol. 33, pp. 116–128, Jan. 2020, doi: 10.1016/j.matpr.2020.03.317.
- [14] W. Li, J. Jaromír Klemeš, Q. Wang, and M. Zeng, “Efficient thermal management strategy of Li-ion battery pack based on sorption heat storage,” *Energy Conversion and Management*, vol. 256, p. 115383, Mar. 2022, doi: 10.1016/j.enconman.2022.115383.
- [15] X. Xu, J. Zhu, H. Zhang, Z. Yi, X. Wang, and G. Zhao, “Low cost energy-efficient preheating of battery module integrated with air cooling based on a heat spreader plate,” *Applied Thermal Engineering*, vol. 232, p. 121024, Sept. 2023, doi: 10.1016/j.applthermaleng.2023.121024.
- [16] M. Ahmadian-Elmi and P. Zhao, “Review of Thermal Management Strategies for Cylindrical Lithium-Ion Battery Packs,” *Batteries*, vol. 10, no. 2, Art. no. 2, Feb. 2024, doi: 10.3390/batteries10020050.
- [17] N. Lee, J. Choi, J. Lee, D. Shin, and S. Um, “Prognostic analysis of thermal interface material effects on anisotropic heat transfer characteristics and state of health of a 21700 cylindrical lithium-ion battery module,” *Journal of Energy Storage*, vol. 72, p. 108594, Nov. 2023, doi: 10.1016/j.est.2023.108594.
- [18] G. Kulkarni, “Comparative Material Selection of Battery Pack Casing for an Electric Vehicle,” *IJRASET*, vol. 11, no. 12, pp. 66–75, Dec. 2023, doi: 10.22214/ijraset.2023.56595.
- [19] U. Lee, N. Kang, and Y. K. Lee, “Optimization of module structure considering mechanical and thermal safety of pouch cell lithium-ion batteries using a reliability-based design optimization approach,” *Journal of Energy Storage*, vol. 72, p. 108650, Nov. 2023, doi: 10.1016/j.est.2023.108650.

- [20] D. Shao *et al.*, “Advanced low-temperature preheating strategies for power lithium-ion batteries applied in electric vehicles: A review,” *International Journal of Electrochemical Science*, vol. 19, no. 11, p. 100817, Nov. 2024, doi: 10.1016/j.ijoes.2024.100817.
- [21] B. Xue, Y. Zhou, P. Chen, X. Meng, and J. Zhang, “Study on Performance of Integrated Thermal Management Strategy for Hybrid Electric Vehicles Under Low-Temperature Conditions,” *Processes*, vol. 13, no. 3, Art. no. 3, Mar. 2025, doi: 10.3390/pr13030651.
- [22] X. Wu, Z. Wei, Y. Sun, J. Sun, and J. Du, “Integrated All-Climate Heating/Cooling System Design and Preheating Strategy for Lithium-Ion Battery Pack,” *Batteries*, vol. 8, no. 10, Art. no. 10, Oct. 2022, doi: 10.3390/batteries8100179.
- [23] Z. Ye, X. Fu, and S. Zhou, “Research on control strategy of rapid preheating for power battery in electric vehicle at low temperatures,” *Applied Thermal Engineering*, vol. 245, p. 122770, May 2024, doi: 10.1016/j.applthermaleng.2024.122770.
- [24] Y. Wang *et al.*, “Low temperature heating methods for lithium-ion batteries: A state-of-art review based on knowledge graph,” *Renewable and Sustainable Energy Reviews*, vol. 213, p. 115389, May 2025, doi: 10.1016/j.rser.2025.115389.
- [25] J. Patel, R. Patel, R. Saxena, and A. Nair, “Experimental investigation of thermal characteristics of a 12S1P Li-ion NMC-21700 battery module under different environments for EV applications,” *International Journal of Thermofluids*, vol. 26, p. 101084, Mar. 2025, doi: 10.1016/j.ijft.2025.101084.
- [26] L. Cai and R. E. White, “Mathematical modeling of a lithium ion battery with thermal effects in COMSOL Inc. Multiphysics (MP) software,” *Journal of Power Sources*, vol. 196, no. 14, pp. 5985–5989, July 2011, doi: 10.1016/j.jpowsour.2011.03.017.
- [27] E. Kaya, L. Reina, and A. d’Adamo, “Investigating the Impact of Varied C-Rates on Lithium-Ion Batteries: A 1D Simulation Study,” *J. Phys.: Conf. Ser.*, vol. 2893, no. 1, p. 012050, Nov. 2024, doi: 10.1088/1742-6596/2893/1/012050.
- [28] D. Nemes, T. Pálfi, and S. Hajdu, “Vehicle Dynamic Simulation Possibilities Using AVL Cruise M,” *International Journal of Engineering and Management Sciences*, vol. 5, no. 2, 2020.
- [29] “Optimize EV battery cell development with parametric design.” Accessed: July 14, 2025. [Online]. Available: <https://engineering.esteco.com/blog/optimize-ev-battery-parametric-design/>

- [30] T.-F. Yang, W.-M. Yan, P.-Y. Lin, C.-Y. Lin, C.-C. Yang, and U. Sajjad, "Thermal management of 21700 Li-ion battery packs: Experimental and numerical investigations," *Applied Thermal Engineering*, vol. 236, p. 121518, Jan. 2024, doi: 10.1016/j.applthermaleng.2023.121518.
- [31] S. Chavan, S. E. Son, B. Venkateswarlu, S. W. Joo, and S. C. Kim, "Impact of external heating and state of charge on discharge performance and thermal runaway risk in 21700 Li-ion batteries," *Case Studies in Thermal Engineering*, vol. 63, p. 105299, Nov. 2024, doi: 10.1016/j.csite.2024.105299.
- [32] P. Cicconi and P. Kumar, "Design approaches for Li-ion battery packs: A review," *Journal of Energy Storage*, vol. 73, p. 109197, Dec. 2023, doi: 10.1016/j.est.2023.109197.
- [33] A. M. Aris and B. Shabani, "An Experimental Study of a Lithium Ion Cell Operation at Low Temperature Conditions," *Energy Procedia*, vol. 110, pp. 128–135, Mar. 2017, doi: 10.1016/j.egypro.2017.03.117.
- [34] Samsung SDI, "Samsung INR21700-50E2 (Data Sheet)." 2018.
- [35] M.-K. Tran *et al.*, "A comprehensive equivalent circuit model for lithium-ion batteries, incorporating the effects of state of health, state of charge, and temperature on model parameters," *Journal of Energy Storage*, vol. 43, p. 103252, Nov. 2021, doi: 10.1016/j.est.2021.103252.
- [36] E. Brorein, "A Deeper Look at Lithium-Ion Cell Internal Resistance Measurements," Keysight. Accessed: June 18, 2025. [Online]. Available: <https://www.keysight.com/blogs/en/tech/bench/2022/05/31/a-deeper-look-at-lithium-ion-cell-internal-resistance-measurements>
- [37] D. A. Pola *et al.*, "Particle-Filtering-Based Discharge Time Prognosis for Lithium-Ion Batteries With a Statistical Characterization of Use Profiles," *IEEE Transactions on Reliability*, vol. 64, no. 2, pp. 710–720, June 2015, doi: 10.1109/TR.2014.2385069.
- [38] D. Natella, S. Onori, and F. Vasca, "An interlaced strategy for open circuit voltage and capacity estimation for lithium-ion batteries," in *2022 IEEE Vehicle Power and Propulsion Conference (VPPC)*, Merced, CA, USA: IEEE, Nov. 2022, pp. 1–6. doi: 10.1109/vppc55846.2022.10003356.
- [39] D. Clerici, F. Pistorio, S. Scalzo, S. Martelli, F. Mocera, and A. Somà, "Mechanical Multiscale Lithium-Ion Battery Modeling for Optimized Battery Pack Design," *Engineering Proceedings*, vol. 85, no. 1, Art. no. 1, 2025, doi: 10.3390/engproc2025085048.

- [40] U. Lee, N. Kang, and Y. K. Lee, "Optimization of module structure considering mechanical and thermal safety of pouch cell lithium-ion batteries using a reliability-based design optimization approach," *Journal of Energy Storage*, vol. 72, p. 108650, Nov. 2023, doi: 10.1016/j.est.2023.108650.
- [41] ARGONNE NATIONAL LABORATORY, "Deliverable Requirements Year 2." BATTERY WORKFORCE CHALLENGE, Apr. 04, 2025.
- [42] A. Rossi, "Case Study: Lithium-Ion Battery Test Enclosure," TotalShield. Accessed: July 09, 2025. [Online]. Available: <https://totalshield.com/blog/case-study-clear-lithium-ion-battery-enclosure/>
- [43] S. Kim, "[INR21700-50G] Cell Specification_BWC Ver.0.0." June 25, 2024.
- [44] Z. Wang, N. Mao, and F. Jiang, "Study on the effect of spacing on thermal runaway propagation for lithium-ion batteries," *J Therm Anal Calorim*, vol. 140, no. 6, pp. 2849–2863, June 2020, doi: 10.1007/s10973-019-09026-6.
- [45] Y. Jiang, J. Huang, P. Xu, and P. Wang, "Axial and radial thermal conductivity measurement of 18,650 Lithium-ion battery," *Journal of Energy Storage*, vol. 72, p. 108516, Nov. 2023, doi: 10.1016/j.est.2023.108516.
- [46] PLASKOLITE, LLC, "TUFFAK® F - FLAME RETARDANT POLYCARBONATE SHEET." 2024. [Online]. Available: https://plaskolite.com/docs/default-source/pds/pds519_tuf_f_eu.pdf
- [47] Celanese, "Thermally Conductive Plastics | CoolPoly® | Celanese." Accessed: July 14, 2025. [Online]. Available: <https://www.celanese.com/products/coolpoly-thermal-conductivity-plastics>
- [48] A. Broatch, B. Pla, P. Bares, and L. Agizza, "Single value decomposition for sparse temperature sensing and state observation in multicell battery packs," *Journal of Energy Storage*, vol. 97, p. 112888, Sept. 2024, doi: 10.1016/j.est.2024.112888.
- [49] Bucan, "Silicone Rubber Heater - Flexible Heater Manufacturers," Bucan. Accessed: July 14, 2025. [Online]. Available: <https://www.bucan.com/silicone-rubber-heaters>

Appendix A

MACCOR Test Sequence

The table below outlines the MACCOR test script used for static capacity testing of 21700 lithium-ion cells under 0 °C ambient conditions. This sequence was developed for the Waterloo team for the Battery Workforce Challenge (BWC) and applied consistently across all test samples to ensure uniform charge-discharge cycling. This test script serves as the baseline protocol for thermal performance of the cells used in this study.

BWC-static-capacity-test.000.000 from BWC_1C_0degC2_192582_April15. Date of printing: 4/15/2024 9:55:13 PM

Test description: This script is for the purpose of BWC cell testing - static capacity test. In the scripts below, please adjust the discharge current value accordingly.

Step	Type	Mode	Value	Limit	Value	End Type	Oper	Value	Goto	Report Type	Value
1	Rest					StepTime	=	00:30:00	002	StepTime	00:03:00
2	Charge	Current	2.45	Voltage	4.2	Voltage	>=	4.2	003	StepTime	00:00:05
3	Charge	Voltage	4.2	Current	2.45	Current	<=	0.245	004	StepTime	00:00:05
4	Rest					StepTime	=	01:30:00	005	StepTime	00:00:05
5	Discharge	Current	4.9	Voltage	2.5	Voltage	<=	2.5	006	StepTime	00:00:01
6	Rest					StepTime	=	01:00:00	007	StepTime	00:01:00
7	Charge	Current	2.4	Voltage	4.2	StepTime	=	00:30:00	008		
8	End										

Figure 24. MACCOR test sequence used for static capacity testing of 21700 li-ion cells at 0 °C

Appendix B

OCV vs SOC curve

This appendix presents the OCV as a function of the SOC used for the ECM plotting. The data was gathered from a static capacity test by discharging a Samsung 21700 lithium-ion cell at a constant C/20 rate. This low current minimizes voltage drops due to internal resistance, allowing accurate approximation of the true OCV profile. The plot serves as the reference OCV–SOC profile for interpolating the voltage at each time step during the ref. ECM model execution. The values are used in the lookup table described in Chapter 3.

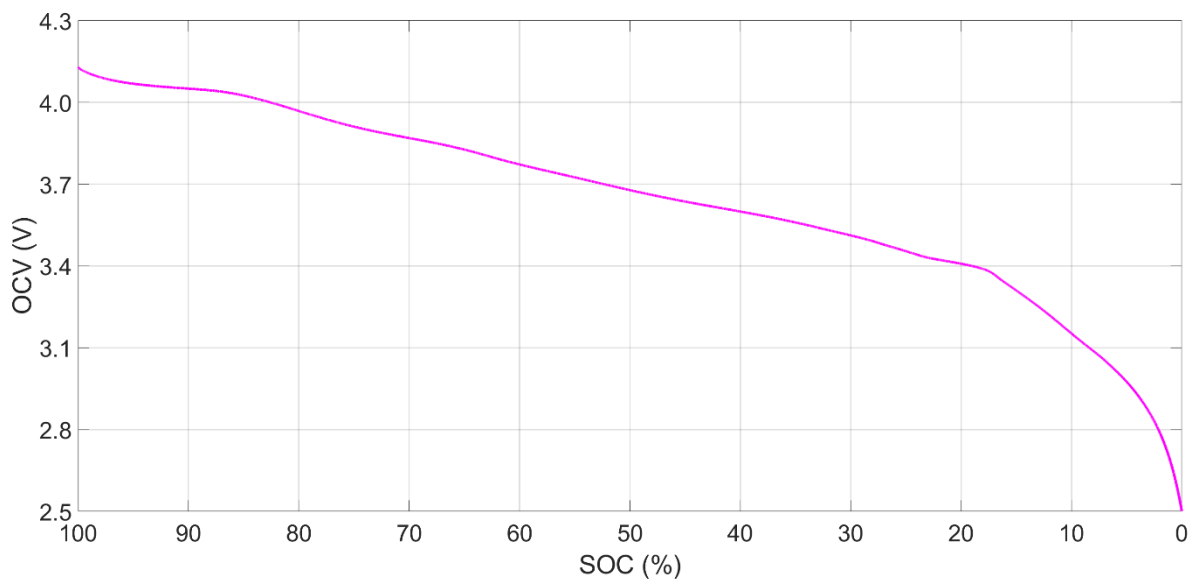


Figure 25. Measured OCV versus SOC curve obtained from a C/20 discharge of a Samsung 21700 li-ion cell.

Appendix C

Module Electrical Configuration

This appendix presents the electrical layout of the battery module used in this study. As shown in Figure 26, the configuration consists of 260 cylindrical cells arranged in a 10s26p format, with parallel cell groupings color-coded and numbered from 1 to 10 to indicate their series connection.

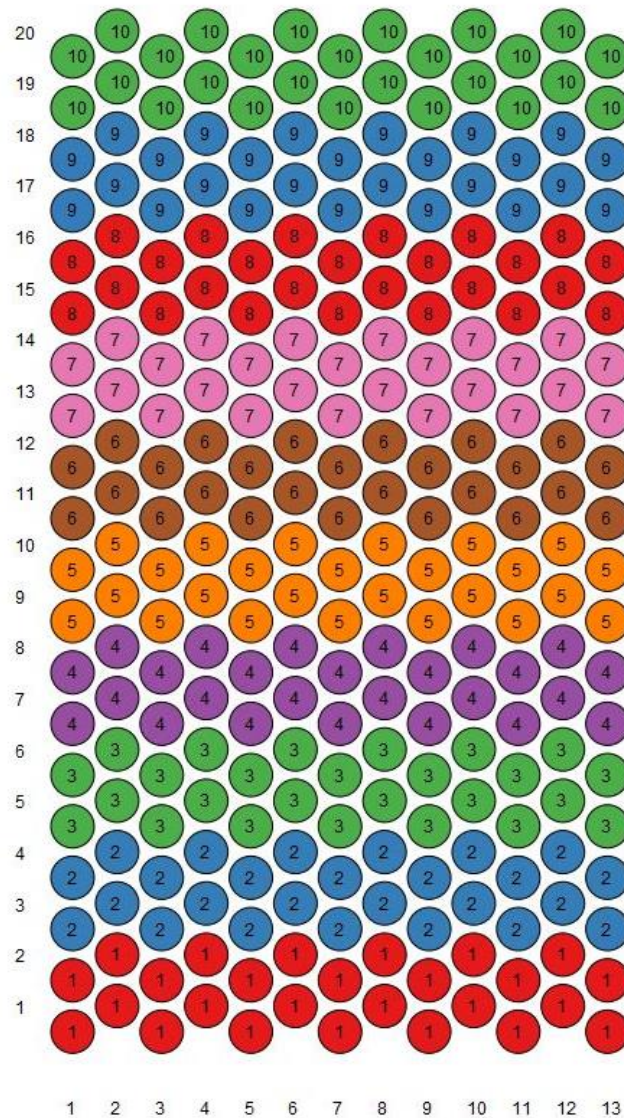


Figure 26. Electrical configuration of a 10s26p cylindrical cell battery module